

# **Geological entropy and solute transport in heterogeneous porous media**

Marco Bianchi<sup>1</sup> and Daniele Pedretti<sup>2</sup>

<sup>1</sup>British Geological Survey, Environmental Science Centre, Keyworth, Nottingham, United Kingdom.

<sup>2</sup>Geological Survey of Finland (GTK), Espoo, Finland

Corresponding author: Marco Bianchi ([marcob@bgs.ac.uk](mailto:marcob@bgs.ac.uk))

## **Key Points:**

- Introduced geological entropy as informative index of spatial disorder of  $K$  field
- Identified relationships between spatial disorder and temporal moments of BTCs
- Knowledge of spatial disorder and variance is sufficient to predict BTC skewness

**Abstract.** We propose a novel approach to link solute transport behavior to the physical heterogeneity of the aquifer, which we fully characterize with two measurable parameters: the variance of the log  $K$  values ( $\sigma_Y^2$ ), and a new indicator ( $H_R$ ) that integrates multiple properties of the  $K$  field into a global measure of spatial disorder or *geological entropy*. From the results of a detailed numerical experiment considering solute transport in  $K$  fields representing realistic distributions of hydrofacies in alluvial aquifers, we identify empirical relationship between the two parameters and the first three central moments of the distributions of arrival times of solute particles at a selected control plane. The analysis of experimental data indicates that the mean and the variance of the solutes arrival times tend to increase with spatial disorder (i.e,  $H_R$  increasing), while highly skewed distributions are observed in more orderly structures (i.e,  $H_R$  decreasing) or at higher  $\sigma_Y^2$ . We found that simple closed-form empirical expressions of the bivariate dependency of skewness on  $H_R$  and  $\sigma_Y^2$  can be used to predict the emergence of non-Fickian transport in  $K$  fields considering a range of structures and heterogeneity levels, some of which based on documented real aquifers. The accuracy of these predictions and in general the results from this study indicate that a description of the global variability and structure of the  $K$  field in terms of variance and geological entropy offers a valid and broadly applicable approach for the interpretation and prediction of transport in heterogeneous porous media.

## 1 Introduction

Solute transport in geological formations is primarily controlled by the spatial distribution of hydraulic conductivity ( $K$ ), which reflects the variability in the textural properties (i.e., grain size, sorting, and particle shape) of the sediments. Stochastic theories have been developed to predict solute behavior in heterogeneous formations characterized by random fluctuations of  $K$  [e.g., Shapiro and Cvetkovic, 1988; Dagan, 1989; Gelhar, 1993; Rubin, 2003; Dagan and Neuman, 2005; Neuman and Tartakovsky, 2009]. Despite promising results in recent years from the application of multiple methods [e.g., Willmann et al., 2008; Fiori and Jankovic, 2012; Flach, 2012; Engdahl et al., 2013; Zhang et al., 2014; Swanson et al., 2015], a general approach has yet to be developed to uniquely link measurable geological properties to input parameters in stochastic models able to predict transport behavior in highly heterogeneous aquifers.

Analytical solutions derived from classical Fickian stochastic theories [e.g., Gelhar and Axness, 1983; Dagan, 1984] do not seem to be universally applicable [e.g., Gómez-Hernández and Wen, 1998]. A possible reason for their poor predictability is that classical stochastic theories rely on a multi-Gaussian representation of the spatial distribution of  $\log K$ , a model that tends to maximize spatial disorder through a minimization of the spatial continuity of extreme values [Journel and Deutsch, 1993]. A great body of work has stressed the impact of the presence and continuity (i.e., connectivity) of extreme  $K$  values (high or low) on solute transport in a variety of depositional environments and at different scales

[Fogg, 1986; Anderson, 1989; LaBolle and Fogg, 2001; Klise et al., 2009; Vassena et al., 2009; Ronayne et al., 2010; Bianchi et al., 2011b; Pedretti et al., 2013].

One important result from numerical experiments of transport in synthetic aquifers characterized by the presence of a well-connected structure is that the simulated temporal distribution of concentrations detected over time at control sections (i.e. breakthrough curves, BTCs) show non-Fickian or “anomalous” features even for small values of the variance of the log  $K$  field ( $\sigma_Y^2$ , where  $Y = \ln K$ ) [Gómez-Hernández and Wen, 1998; Wen and Gómez-Hernández, 1998; Zheng and Gorelick, 2003; Zinn and Harvey, 2003; Liu et al., 2004; Teles et al., 2004; Willmann et al., 2008; Fiori et al., 2010]. These anomalous features include faster-than-expected breakthrough of concentrations at controlling sections, asymmetric and multi-peaked BTCs, and pronounced post-peak (late-time) behavior or *tailing*. Experimental evidences of anomalous BTCs in laboratory and field experiments were reported for instance by *Bianchi et al.* [2011a], *Boggs et al.* [1992], [*Cherubini et al.*, 2013; *Molinari et al.*, 2015; *Pedretti et al.*, 2016].

We contend in this work that a description of the structure of the  $K$  field in term of spatial disorder offers a valid and broadly applicable approach for the interpretation and prediction of transport in heterogeneous porous media. In specific, transport is more closely adherent to the Fickian interpretation in  $K$  fields characterized by a high degree of spatial disorder (*high geological entropy*), while

non-Fickian features emerge in more orderly structures (*low geological entropy*). The validity of this hypothesis is evaluated in this paper with a stochastic numerical experiment in which we compare fundamental characteristics of solute transport behavior, such as the temporal moments of BTCs, to heterogeneous aquifer scenarios in which geological complexity is fully controlled by two measurable parameters: a new index of spatial disorder ( $H_R$ ) of the structure of  $Y$  and its global variance ( $\sigma_Y^2$ ). The experiment focuses on alluvial aquifers with intermediate (orders of few meters) to moderately large (order of few tens of meters) spatial scale of  $K$  variations. As a working approach, it is assumed that this variability is the result of the spatial distribution of hydrofacies associated with the depositional elements of a typical alluvial aquifer. Therefore, the  $K$  fields considered here are mapped on the basis of stochastic realizations of the spatial distribution of hydrofacies generated with a transition probability/Markov Chain approach [Carle and Fogg, 1996, 1997]. With this approach, the  $K$  structure of the aquifer is consistent with the geological and sedimentological setting [e.g., Fogg, 1986; Anderson, 1989; Allen-King et al., 1998; Fogg et al., 1998; Riva et al., 2008; Zhang et al., 2013; Bianchi and Zheng, 2016].

We consider several testing scenarios with different level of  $K$  heterogeneity and spatial disorder including five scenarios that mimic the conditions of real alluvial aquifers known in the literature [LaBolle and Fogg, 2001; Zhang et al., 2013; Bianchi and Zheng, 2016]. Based on analysis of the ensemble of results obtained from the numerical experiment, our goal is to prove that simple closed-

form expressions could be derived to relate  $(H_R, \sigma_Y^2)$  pairs to metrics describing transport behavior in different settings of aquifer heterogeneity. In this regard, we focus on the third central moment or skewness of the BTCs, which is a descriptor of non-Fickian transport on the basis of the degree of tailing.

This paper is structured as follows. Section 2 introduces the concept of geological entropy with an illustrative example. Section 3 describes methodology for calculating the indicator  $H_R$ . Here, we also describe the numerical experiment to assess the impact of  $H_R$  on solute transport behavior. Section 4 analyses and discusses the main results from the experiment, focusing on empirical relationships between the temporal moments of the simulated BTCs and  $H_R$ . Section 5 focuses on the ability of these relationships to predict anomalous transport. A discussion is presented in Section 6 to explore the analogies and differences between the concepts of geological entropy and connectivity. The conclusions drawn from this study are presented in Section 6.

## **2 An illustrative example**

Before venturing into the derivation of geological entropy indicators and the explanation of the testing methodology, we first present a simple and explanatory example to introduce the concept behind this work. The example is graphically illustrated in Figure 1. Two 2-D flow and transport simulations based on a particle-tracking approach were generated and analyzed. Both aquifers are confined with groundwater flowing from left to right according to the same mean

hydraulic gradient as imposed by identical specified head boundary conditions and model geometry for the two systems. We discretized a solute mass  $M$  into a number of particles  $n_p$ , which were instantaneously injected at time  $t_0$  along a vertical line located at a certain position in the aquifer (identical in the two systems). Solute BTCs in the two aquifers were analyzed in the form of cumulative density functions (CDFs) of particles' arrival times measured at a control section downgradient of the injection line. For this illustrative example, we assume that particles moves only by advection, and exit the system when they reach the right boundary.

The two systems are characterized by identical proportions of two hydrofacies and embed the same bimodal  $K$  distribution ( $K$  contrast equal to  $10^2$ ). The only difference is the spatial organization of the hydrofacies, which in turn is associated with a different degree of geological entropy. This entropy is larger for the disorderly or chaotic system at the top of Figure 1 than in the orderly or less chaotic system at the bottom. Note that in both systems, the proportion of the facies with higher conductivity (Facies 2) is lower than the percolation threshold [Stauffer and Aharony, 1994; Harter, 2005], meaning that there are not continuous high- $K$  features (channel or block) spanning the entire system from left to right. Visual inspection of Figure 1 also suggests that Facies 2 does not appear to be significantly "more connected" in the orderly system. In fact, although the number of clusters of this facies is smaller in the orderly system,

clusters are generally small and isolated within lower  $K$  matrix (Facies 1) in both systems.

Notwithstanding these similarities, the distributions of the particles' arrival times differ significantly between the two systems. In particular, the CDF in the orderly system shows that the arrival times distribution is more skewed to the right (i.e., the median arrival time of the particles is lower than the mean arrival time  $\bar{t}$ ) and displays stronger tailing effects than that in the disorderly system, where arrival times are more symmetrically distributed around  $\bar{t}$ . Readers familiar with stochastic theories may intuitively associate this difference in CDF scaling to the different homogenization of the system. Compared to the orderly system, particles experienced a larger number of heterogeneity transitions in the disorderly system, which promote mixing and dispersion of the particles arriving at the controlling section.

The key point here is that, differently from traditional stochastic theories and previous investigations focusing solely on connectivity of extreme  $K$  values, we relate transport behavior in the two systems to their geological entropy. In the next sections we will define a unique indicator ( $H_R$ ) to quantify this property of the medium. By elaborating on more complex examples than those presented in Figure 1, we will also define empirical relationships describing the dependency of transport on this measurable metric.

### 3 Methods

#### 3.1 Quantification of geological entropy and derivation of $H_R$

The proposed indicator of geological entropy is based on the concept of Shannon information entropy [Shannon, 1948], which has been used in the past to quantify complexity and randomness in various scientific fields including statistical mechanics and fluid dynamics [Jaynes, 1957; Ottino, 1990], hydrology [Martina and Entekhabi, 2006; Singh, 2011; Castillo et al., 2015], image processing [Barba et al., 1989; Wu et al., 2013], geography and spatial statistics [Batty et al., 2014; Leibovici et al., 2014], and landscape ecology [Vranken et al., 2015], just to name a few. Information entropy concepts have also been applied to quantify the uncertainty of geological models [Elfeki and Dekking, 2005; Huang et al., 2012; Wellmann and Regenauer-Lieb, 2012; Bianchi et al., 2015], and to describe the spatial and temporal variability of solute plumes [Woodbury and Urych, 1993; Kitanidis, 1994; Gotovac et al., 2010; Chiogna et al., 2012], as well as of infiltration processes in unsaturated heterogeneous soils [Mays et al., 2002]. Journel and Deutsch [1993] used a bivariate entropy index to measure and compare the spatial disorder of stochastic realizations of a permeability field based on multi-Gaussian, sequential indicator, and mosaic geostatistical models. Simulations of fluid flow showed that the model with the maximum spatial disorder (i.e., the multi-Gaussian), which in principle should be preferable from a Bayesian point of view [Christakos, 1990], does not provide maximum entropy responses from the flow model (e.g., effective  $K$  values).

We start by defining the *global* entropy of a discrete random variable  $F$  representing a set of  $N$  hydrofacies. From the definition of Shannon information entropy, this can be expressed with the following:

$$H_G = -\sum_{n=1}^N p_{G,n} [\ln p_{G,n}] \quad (1)$$

where  $p_G$  are the volumetric proportions of the hydrofacies over the domain of interest. The number and the volumetric proportions of the hydrofacies can be estimated from the analysis of geological data (e.g., borehole logs).  $H_G$  ranges from a minimum of 0, when  $N=1$ , to a maximum value when  $p_G = 1/N$  for every outcome value of  $F$  (i.e., uniform distribution). This maximum value ( $H_{MAX}$ ) is given by:

$$H_{MAX} = -\sum_{n=1}^N p_{G,n} [\ln p_{G,n}] = -N \frac{1}{N} \left[ \ln \frac{1}{N} \right] = \ln N \quad (2)$$

Let us now assume that the spatial distribution of  $F$  has been defined over a grid covering the domain of interest. For each grid block, we can calculate the *local* entropy  $H_L$  according to the following:

$$H_L(l) = -\sum_{n=1}^N p_{l,n} [\ln p_{l,n}] \quad (3)$$

where  $p_l$  are the marginal probabilities of the outcome values of  $F$  calculated within a subdomain of length  $l$  centered around the grid block. Similarly to  $H_G$ ,  $H_L(l)$  is defined within the interval  $[0, H_{MAX}]$  where  $H_{MAX}$  is given by Equation 2. Local entropy values depend on the dimensions of the subdomain. The average of these values over the entire domain tends to rapidly increase (more disorder) with  $l$ , and asymptotically approaches  $H_G$  regardless of the structure of the  $F$  field

(see Figure S1 in the Supporting Information (SI) accompanying the paper).

Therefore, we focus on spatial disorder at the local scale to characterize the geological entropy of the  $F$  field, and we use a length  $l$  equal to three times the dimension of the grid blocks in each direction. With this choice, the marginal probabilities  $p_l$  are calculated over a set of 27 blocks for a 3-D grid (this number would reduce to 9 for a 2-D grid). The definition of local entropy highlights the difference between our approach and the bivariate entropy of *Journal and Deutsch* [1993]. In particular, in the calculation of the marginal probabilities  $p_l$  in Equation 3, the occurrences of the outcomes of  $F$  within the subdomain are considered as independent events, while in the definition of bivariate entropy these probabilities are treated as joint probabilities of the outcomes of the two random variables  $F(\mathbf{u})$  and  $F(\mathbf{u}+\mathbf{h})$ , where  $\mathbf{u}$  and  $\mathbf{u}+\mathbf{h}$  are position vectors.

By combining the definitions of global and local entropy, we define the *relative* entropy index  $H_R$  with the following equation:

$$H_R = \frac{\overline{H_L}}{H_G} \quad (4)$$

where  $\overline{H_L}$  is the average of the local entropy over the entire domain. For a 3-D grid with  $I$ ,  $J$ , and  $K$  numbers of elements along Cartesian axes,  $\overline{H_L}$  is given by

$$\overline{H_L} = \frac{1}{I \times J \times K} \sum_{k=1}^K \sum_{i=1}^I \sum_{j=1}^J H_L(i, j, k) \quad (5)$$

The relative entropy index  $H_R$ , which belongs to the interval  $[0, 1]$ , provides a quantitative measure of the spatial disorder of  $F$ . In particular,  $H_R$  values close to

1 (i.e.,  $\overline{H}_L \approx H_G$ ) indicate that the marginal probabilities  $p_i$  of the outcome values of  $F$  at the local scale are similar to the global probabilities or volumetric proportions  $p_G$  over the entire domain. This is indicative of a disorderly structure as the one shown on the top left panel of Figure 2, which was generated by randomly assigning three possible hydrofacies (i.e., A, B, and C) to the blocks of a 2-D grid. As a result of the high level of disorder,  $H_L$  values are close to the maximum value (i.e.,  $\ln[3]$ ) in the vast majority of the domain (bottom left panel), and consequentially the  $H_R$  index for this field is equal to 0.85. Conversely, low values of  $H_R$  (i.e.,  $\overline{H}_L \ll H_G$ ) indicate that one of the hydrofacies is generally more frequent over the others at the local scale. This is indicative of an orderly structure such as when there are large volumes (in 3-D) or areas (in 2-D) of the domain characterized by the same hydrofacies. An example of such structure characterizes the field in the top right panel of Figure 2, which has a very low  $H_R$  index (0.09).

Two key aspects of the index  $H_R$  are as follows. The first is that  $H_R$  is directly related to measurable aquifer properties including the number and volumetric proportions of the hydrofacies over the domain of interest. All these properties can be measured by conventional methods of geological investigation. The second aspect is that,  $H_R$  is a global metric that takes into account multiple properties of the  $K$  field (e.g., connectivity, volumetric proportions of the different hydrofacies, correlation lengths, etc.). In particular, because  $H_R$  is a function of the global entropy, it provides unbiased estimations of disorder even if a category

is significantly more frequent than the others.  $H_R$  is also sensitive with respect to spatial correlation structure of the variable of interest, as well as to the connectivity and spatial continuity of certain  $K$  values. A more specific discussion highlighting similarities and differences between geological entropy and connectivity concepts is presented in Section 5.

### **3.2 Testing methodology**

Our aim is to explore the existence of a quantitative link between geological entropy and transport in heterogeneous  $K$  fields. To this end, we developed a Monte Carlo (MC) framework based on the solution of flow and transport in independent and identically distributed realizations of the spatial distribution of three hydrofacies, representing a wide range of realistic geological structures.

#### *3.2.1 Scenarios of aquifer heterogeneity*

The adopted conceptual model of aquifer heterogeneity considers the spatial distribution of three hydrofacies chosen to represent the main deposits typically encountered in alluvial aquifers. These include fine-grained and generally low conductivity floodplain deposits (hydrofacies LK), coarse-grained and generally high conductivity channel fills (hydrofacies HK), and deposits with intermediate characteristics such as levees and/or crevasse splays (hydrofacies IK). The nomenclature for the hydrofacies is simply based on their hydraulic conductivity, and in particular “L” stands for low, “I” stands for intermediate, and “H” stands for high. Accordingly,  $K_{LK}$ ,  $K_{IK}$ , and  $K_{HK}$  indicate the characteristic hydraulic conductivity of hydrofacies LK, IK and HK, respectively.

Random realizations of the spatial assemblage of the three hydrofacies are generated with a transition probability/Markov chain approach (T-PROGS; Carle, 1999). This established geostatistical method has been applied to simulate the distribution of geological units in a variety of depositional environments [Fogg *et al.*, 1998; Weissmann *et al.*, 1999; Lee *et al.*, 2007; Bakshevskaya and Pozdniakov, 2015; Bianchi *et al.*, 2015; Siirila-Woodburn and Maxwell, 2015; Zhu *et al.*, 2015; Bianchi and Zheng, 2016]. With the transition probability approach, realistic representations of the hydrofacies architecture are generated on the basis of measurable geological properties such as the number and the volumetric proportions of the hydrofacies, their mean lengths along specific directions, and their juxtapositional tendencies. All these properties are in fact considered in the implementation of a Markov chain model of the spatial structure of the categorical variable representing the different hydrofacies. Unlike variogram-based geostatistical methods, the spatial structure in T-PROGS is defined on the basis of a set of transition probabilities between hydrofacies, each defining the conditional probability of one hydrofacies to occur adjacent another along a particular direction. Implemented Markov chain models are used by a stochastic simulation algorithm in which a preliminary spatial configuration of the hydrofacies, based on sequential indicator simulation (SIS, Deutsch and Journel, 1998) is modified in a successive optimization step to improve the match between measured and simulated transition probabilities. A comprehensive description of the T-PROGS algorithm for generating stochastic simulations of

categorical variables is provided by *Carle and Fogg* [1996, 1997] and *Carle* [1999].

We consider six groups of scenarios of aquifer heterogeneity (summed up in Table 1). For each scenario, 100 MC realizations of the spatial distribution of the three hydrofacies are generated considering a Cartesian 3-D grid with dimensions of 200 m, 300 m, and 40 m in the  $x$ ,  $y$ , and  $z$  directions, respectively. The size each grid block is equal to 1 m in the  $x$  and  $y$  directions, and to 0.5 m in the vertical ( $z$ ) direction, for a total about  $4.8 \times 10^6$  grid blocks. Transition probabilities between hydrofacies for the development of the Markov chain models for all the groups are chosen to favor a fining-upward tendency commonly observed in fluvial deposits [e.g., *Miall*, 2014] while cross-transition probabilities in the horizontal directions ( $x$  and  $y$ ) are assumed equal to the corresponding probabilities in the  $z$  vertical direction in accordance with Walther's Law [*Fogg et al.*, 1998]. Examples of generated MC realizations are presented in Figures S2 – S5 of the Supporting Information (SI) accompanying the paper.

Group 1 considers nine scenarios representing an alluvial-like aquifer characterized by the predominance of low  $K$  sediments (volumetric fraction of hydrofacies LK is equal to 0.6). Hydrofacies IK and HK are embedded in the lower  $K$  matrix, and have similar volumetric proportions (0.2). On the basis of these proportions among hydrofacies, the global entropy  $H_G$  of all the scenarios in this group is equal to 0.950 (Equation 1). It is also assumed that there is a difference of three orders of magnitude between  $K_{HK}$  and  $K_{HL}$ , and of two orders

of magnitude between  $K_{HK}$  and  $K_{IL}$ . Accordingly, all the  $K$  fields in this group are characterized by a three-modal distribution of the  $K$  values with the same fixed variance  $\sigma_Y^2 = 7.3$ . The nine scenarios in Group 1 differ with respect to the isotropic horizontal mean length of hydrofacies HK and IK (i.e.,  $L_x = L_y = L_h$ ), which ranges from 1 m up to 30 m. By changing the facies length, we impose variations in geological entropy for each scenario as shown by the relative entropy  $H_R$  values reported in Table 1.

Scenarios in Group 2 consider similar variations in  $L_h$ . However,  $K$  fields in this group are dominated by the highly conductive sediments of hydrofacies HK (0.6 in volumetric fraction), with lower fractions of less conductive material embedded (0.2 for both hydrofacies LK and IK). Contrasts in  $K$  between the hydrofacies in this group are the same as those in Group 1, resulting in variance  $\sigma_Y^2 = 8.6$  for all the scenarios.

Groups 3, 4, and 5 assume scenarios with identical volumetric proportions for the three hydrofacies ( $p_G = 1/3$ ), a condition that maximizes global entropy  $H_G$  for a system with three categories. Within each group we evaluate five different values of  $\sigma_Y^2$  (i.e., 1.7, 4.7, 10.1, 17.9, 28.0) by changing the contrast in  $K$  between hydrofacies HK and LK from a minimum of 2 up to a maximum of  $2 \times 10^5$  (Figure 3b), while the  $K$  contrast between hydrofacies HK and IK is kept constant and equal to one order of magnitude in all the scenarios.

The last group (Group 6) consists of five scenarios in which the volumetric proportion of hydrofacies HK, the mean lengths of hydrofacies HK and IK, as well

as the  $K$  contrasts between hydrofacies are kept constant, while we change the volumetric proportions of hydrofacies IK and LK. This generates scenarios in which both variance and  $H_R$  change by pairs (Figure 3c). More details about this group are provided in the SI.

### 3.2.2 Flow and solute transport simulations

Saturated groundwater flow in the generated synthetic  $K$  fields is simulated with the three-dimensional finite-difference code MODFLOW-2005 [Harbaugh, 2005] under steady state conditions. The location and size of the blocks in numerical grid correspond to those of the geostatistical grid. Dirichlet (specified head) boundary conditions are assigned to two sides of the domain, and no flow conditions to the other sides (Figure 4). Accordingly, the mean flow direction is approximately parallel to the  $y$  axis. Specified head values are set up to generate a mean hydraulic gradient  $I$  equal to 0.001.

Conservative solute transport is simulated using the advection dispersion equation, resolved in a Lagrangian scheme using the random-walk particle-tracking code RW3D, a well-known code used in multiple applications involving transport in heterogeneous media [Fernández-García *et al.*, 2005; Salamon *et al.*, 2006]. We assumed constant porosity for all the hydrofacies (0.1), an isotropic small local dispersivity of 0.01 m, and an effective molecular diffusion coefficient equal to  $5.2 \times 10^{-5}$  m<sup>2</sup>/day, which is the same as the value used in previous studies considering  $K$  contrasts between hydrofacies within the range of values assumed in this study [e.g., [LaBolle and Fogg, 2001; Zhang *et al.*, 2007,

2013]. These assumptions are made to avoid a possible bias in the interpretation of the results due to overlapping of complex transport mechanisms (e.g. the impact of transversal dispersion). Our primary goal is indeed to explore the response of the transport solution to the random variability of the seepage velocity vector due to the variability and entropy-controlled structure of the  $K$  field. The analysis of the impact of different Péclet numbers and transversal dispersion on the relationships between geological entropy and anomalous transport is left open for a future development.

The adopted injection scheme mimics a natural gradient field test in which a pulse of a conservative solute is injected in the aquifer through a fully-penetrating passive borehole. Particles were instantaneously released in the domain along an injection line located at a point of coordinates 100 m ( $x$ ) and 50 m ( $y$ ), as shown in Figure 4. The vertical profile of  $K$  along the injection line is shared by all the scenarios within in each group. This was done by conditioning the T-PROGS simulations to the same vertical distribution of hydrofacies for all the scenarios within each group. The number of particles entering the domain is proportional to the local velocity flux to better represent flux-averaged conditions. After a sensitivity analysis, we found that  $10^4$  is a suitable number of particles for computationally efficient and accurate solutions of the transport equations.

We measured the temporal moments of the distribution of travel times of the ensemble of released particles crossing the outflow boundary of the flow model domain, which is located at a distance of 250 m (downgradient) from the injection

line. The resulting residence cumulative distribution functions (CDFs) were transformed into resident solute BTCs using the adaptive kernel density estimator described by *Pedretti and Fernández-García* [2013].

## 4 Results and analysis

### 4.1 Geological entropy of the synthetic $K$ fields

Using the indicators described in Section 3.1, geological entropy was measured for the considered scenarios of aquifer heterogeneity. Plots of the spatial distribution of the local entropy  $H_L$  (Equation 3) for selected  $K$  fields are presented in Figures S2 – S5 (SI). By comparing the distributions of  $H_L$  and the corresponding spatial distribution of the hydrofacies, it is clear that this parameter is effective in identifying 3-D sectors of the domain characterized by different degrees of spatial disorder. The relative entropy index  $H_R$  integrates this information about the structure of the fields into a single metric, which allows to make comparisons between fields with different structures.

An example of this type of comparison is shown in Figure 3a for the scenarios of Group 1 and 2. In both groups,  $H_R$  decreases with the isotropic mean length of the hydrofacies ( $L_h$ ) according to a relationship that can be best described as:

$$H_R = aL_h^b \quad (6)$$

where the constant  $a$  is positive and the exponent  $b$  is negative. Accordingly, the  $K$  field structure becomes more organized or less chaotic as the mean length of

hydrofacies increases. The difference in the values of  $H_R$  between the two groups indicates that the relationship between  $H_R$  and  $L_h$  depends the volumetric proportions of the hydrofacies, and therefore on the type of aquifer.

In a way similar to the first two groups, the geological entropy of the scenarios in Group 3, 4 and 5 is consistent with the assumed hydrofacies architecture, with  $H_R$  values equal to about 0.7, 0.4, and 0.3, respectively (Table 1).

## 4.2 Linking geological entropy and transport behavior

In this work, we used two measurable parameters (i.e.,  $H_R$  and  $\sigma_Y^2$ ) to describe the heterogeneity of a  $K$  field. The new index  $H_R$  provides information about the structure of the field, while the variance  $\sigma_Y^2$  measures the variability of the  $K$  values. We now show that these two parameters are linked to the results of our numerical experiment. We first analyze the groups of scenarios with variable  $H_R$  and constant  $\sigma_Y^2$  (Groups 1 and 2), and then the group of simulations with constant  $H_R$  and variable  $\sigma_Y^2$  (Groups 3, 4, and 5). Results for the group of scenarios in which both  $H_R$  and constant  $\sigma_Y^2$  are variable (Group 6) are documented in the SI as further validation of the results obtained in the previous groups.

### 4.2.1 Scenarios with variable $H_R$ and constant $\sigma_Y^2$

The ensemble of solute BTCs for two scenarios of Group 1 and 2 are plotted in Figure 5, while the arithmetic mean values of the ensemble BTCs for five

selected scenarios in each group are presented in Figures S6 (Group 1) and S7 (Group 2) in the SI. In all the figures, BTCs are plotted in log-log scale to emphasize the presence of power-law-like patterns on the distribution tails. BTCs in Figures S6 and S7 are also normalized by the mean arrival times to highlight the asymmetry in the shape of the BTCs. BTCs are unequivocally more asymmetric and right-skewed for scenarios characterized by low  $H_R$  values. In these scenarios, the late-time portions of the BTCs also show a power-law-like scaling (Figure 5b and 5d), while BTCs calculated for fields with higher  $H_R$  show a relatively symmetric shape and less pronounced tailing (Figure 5b and 5d).

These qualitative considerations about the relationship between  $H_R$  and solute transport behavior are confirmed by the analysis of the first three central temporal moments of the BTCs representing the mean ( $\mu_t$ ), the variance ( $\sigma_t^2$ ), and the skewness ( $sk_t$ ) of the distribution of arrival times at the control plane. Boxplots of the distributions of the moments calculated for each of the generated  $K$  fields are presented in Figure S10 (SI).

The median values the distributions of calculated moments are presented in Figure 6, which suggests clearly identifiable dependencies between the moments and  $H_R$ . In particular, three empirical relationships seem to best describe these dependencies:

$$\tilde{\mu}_t = a[H_R]^b \quad (7)$$

$$\tilde{\sigma}_t^2 = a + b[\ln H_R] \quad (8)$$

$$\tilde{sk}_t = a[H_R]^b \quad (9)$$

where the symbol  $\tilde{\phantom{x}}$  indicates the median value of the distributions of temporal moments. The values of parameters  $a$  and  $b$  differ for each moment. Best fit curves of these equations are plotted as dashed lines in Figure 6. For both Group 1 and Group 2, the mean and variance of the arrival times tend to increase monotonically with spatial disorder (i.e.,  $H_R$  increasing). This is because in a disorderly structure particles travel within a certain  $K$  zone for short distances after which they undergo to transitions into a different  $K$  zone. The number of these transitions becomes larger with higher spatial disorder also causing higher dispersion in the particle arrival times. Moreover, spatial disorder also increases the probability of the particles to travel through low- $K$  zones, which explains the increasing delay in the mean arrival times with  $H_R$ . The increment in median skewness values as  $H_R$  decreases indicates that the tailing of the BTCs becomes heavier as the structures of the  $K$  fields become more orderly. In orderly structures, the presence of preferential flow paths within high  $K$  zones, as well as of large low  $K$  areas where particles can linger for long times, result in asymmetrical arrival time distributions. Conversely, particle paths mix more frequently in disorderly structures with the result of producing symmetric distributions.

#### 4.2.2 Scenarios with constant $H_R$ and variable $\sigma_Y^2$

The ensemble BTCs for the scenarios in Groups 3, 4, and 5 are plotted in Figure S8 (SI). By comparing the shape of the BTCs within each group (i.e., for a fixed  $H_R$  value), it is clear that the shape of the BTC becomes progressively more

asymmetric and irregularly shaped for larger  $\sigma_Y^2$  values. This result suggests that a characterization of the structure solely in terms of geological entropy is not sufficient to characterize transport behavior. However, the comparison of BTCs from scenarios with identical  $\sigma_Y^2$  further confirms of the high impact of  $H_R$  on transport. In fact, we observe systematically heavier tails in the BTCs for the scenarios in Group 5 ( $H_R = 0.29$ ), while more symmetric distributions and less pronounced tailing are associated with the two groups with higher geological entropy. It is significant that, while power-law like scaling in the tails of the BTCs is observed for scenarios in Group 4 and 5, this behavior is never attained for the highly disorderly scenarios in Group 1 ( $H_R = 0.68$ ) regardless of variance  $\sigma_Y^2$ . By recalling that the multi-Gaussian structure is a spatial configuration that maximizes disorder, this result provide an explanation for the absence of anomalous features in BTCs from simulations considering multi-Gaussian  $K$  fields, unless some artificial conditioning is done to enhance system's connectivity and therefore spatial order [e.g., Zinn and Harvey, 2003; Willmann et al., 2008].

Median values of the temporal moments for the three groups are plotted in Figure 7 for different  $\sigma_Y^2$  values, while boxplots of the distributions of the moments are provided in the SI (Figure S11). In all the groups, median values of  $\mu_t$  and  $\sigma_t^2$  increase with the variance of the  $K$  field, according to relationships that can be best described by exponential functions in the form:

$$\frac{\widetilde{\mu}_t}{t_{eq}} = \exp[a\sigma_Y^2] \quad (10)$$

$$\widetilde{\sigma}_t^2 = \exp[a(\sigma_Y^2)^b] \quad (11)$$

Where  $a$  and  $b$  are positive parameters, and  $t_{eq}$  is the arrival time of the particles in an homogenous field with constant  $K$  equal to the equivalent conductivity ( $K_{eq}$ ) of the heterogeneous field [Renard and de Marsily, 1997; Sanchez-Vila et al., 2006]. For the domain of interest, the equivalent conductivity is defined by  $K_{eq} = -QL/A\Delta h$  where  $Q$  is the total flow rate crossing the outflow boundary,  $L$  is the distance between sided with prescribed heads,  $\Delta h$  is the head difference, and  $A$  is cross-sectional area. It is noteworthy that very similar values of  $\widetilde{\sigma}_t^2$  are obtained for all the groups suggesting that, for a given set of volumetric fractions of the hydrofacies, the median variance of the distribution of arrival times is not very sensitive to the structure of the  $K$  field (Figure 7b).

Our results show that empirical exponential functions can also be fitted to data to describe the relationship between  $\sigma_Y^2$  and  $sk_t$ . These can be written as:

$$\widetilde{sk}_t = \alpha(1 - \exp[\beta\sigma_Y^2]) \quad (12)$$

where parameter  $\alpha$  is positive and  $\beta$  is negative. The goodness-of-fit of the best-fitted functions (Figure 7c) is adequate as indicated by the values of the coefficient of determination ( $R^2$ ) between 0.929 and 0.975.

We also found from our experimental datasets that the best-fitted values of the exponent  $\beta$  in Equation 12 are actually very similar for all the groups (mean -0.10, variance  $\approx 10^{-5}$ ), while the values of the parameter  $\alpha$  strongly

correlate with the  $H_R$  values of the three groups of scenarios (Figure S13 in the SI). The correlation between  $\alpha$  and  $H_R$  ( $R^2 = 0.998$ ) is best described by the following:

$$\alpha = 1.99[H_R]^{-1.54} \quad (13)$$

Substituting (13) into (12), and taking the exponent  $\beta$  as a constant, we obtained the following closed-form expression:

$$\widetilde{sk}_t = 1.99 \left( 1 - \exp \left[ -\frac{\sigma_Y^2}{10} \right] \right) H_R^{-1.54} \quad (14)$$

which allows us to predict the median skewness of solute BTCs solely from geological entropy  $H_R$  and the total  $\ln K$  variance  $\sigma_Y^2$ . This empirical solution is highly valuable because it is free of any fitting parameter, since depends exclusively on two measurable parameters to describe the heterogeneity of the  $K$  field. For any aquifer, values of these parameters can be obtained from (hydro)geological data and a representation of the spatial distribution of the hydrofacies or  $K$  classes over the domain of interest.

### 4.3 Testing the predictability of Equation 14

To test the predictability of Equation (14), we considered validation data from a number of scenarios of aquifer heterogeneity. Because the empirical parameters in Equation (14) were obtained only from the analysis of Groups 3-5, a first set of validation data includes the results from Groups 1, 2, and 6. A second set of validation data is based instead on the results of additional transport simulations in  $K$  fields representing real and synthetic aquifers

described in the literature. To provide a unique framework to compare the predictive ability of Equation (14), we built a set of curves expressing the relationship between  $\sigma_Y^2$  and  $sk_t$  for a number of  $H_R$  values, ranging from 0.1 to 1. On top of these curves, shown as gray dashed lines in Figure 8, we overlapped the first set of validation data (Groups 1, 2, and 6) as blue symbols and the second set (documented case studies) as red symbols.

The real and synthetic aquifers used for generating the second set of validation data include:

- the aquifer at the MADE site [Zheng *et al.*, 2011], as per the lithological model presented by Bianchi and Zheng [2016];
- the aquifer at the Lawrence Livermore National Laboratory (LLNL P18), as per the statistical parameters of the hydrofacies models presented by Fogg *et al.* [1998], LaBolle and Fogg [2001], and Zhang *et al.* [2013];
- the alluvial fan of the River Brenta near the Venice Lagoon (VL) in northeastern Italy [Beretta and Terrenghi, 2016], as per the lithofacies model by [Terrenghi *et al.*, 2016];
- two synthetic aquifers (LLNL P48 and LLNL P48\_05), as per the hydrofacies models by Zhang *et al.* [2013] based on a modification of the original parameters of the LLNL aquifer.

For each case study, hydrofacies models were generated according to site-specific T-PROGS input parameters (e.g., number of hydrofacies, transition probabilities, and mean lengths) extracted from relevant bibliographic references,

and then one hundred stochastic transport simulations were performed using the previously described numerical framework. Due to the similarity between the scales of the domain of our modeling framework and the average scale of the analyzed case studies, we did not perform an upscaling or downscaling of the mean lengths of the hydrofacies.

Calculated  $H_R$  values for these case studies indicate a range of geological entropy in the  $K$  field structures between low and high, while  $\sigma_Y^2$  values are representative of variable degrees of heterogeneity in the  $K$  distributions (Table 2). In particular,  $K$  fields representing the type of heterogeneity observed at the aquifers at the MADE site and at LLNL are characterized by a very orderly structure ( $H_R \approx 0.3$ ), although the values of  $\sigma_Y^2$  for the two case studies are very different. The  $K$  fields based on the synthetic aquifers of Zhang et al. [2013] have the same very high variance  $\sigma_Y^2$ , but differ in terms of  $H_R$  values (0.42 vs. 0.74), as the structure for LLNL P48\_05 is much more chaotic. The  $K$  fields for the case similar to the VL aquifer are characterized by intermediate  $H_R$  and  $\sigma_Y^2$  values with respect to the other analyzed case studies.

BTCs resulting from transport simulations are extremely skewed ( $\widetilde{sk}_t = 12.5$ ) for the LLNL P18 case study, highly skewed ( $\widetilde{sk}_t \approx 7$ ) for LLNL P48, and skewed ( $\widetilde{sk}_t \approx 3$ ) for all the remaining case studies regardless of the large differences in  $\sigma_Y^2$ . These results highlight once again the impact of  $H_R$  on transport behavior, along with  $\sigma_Y^2$ . This is particularly evident from the analysis of the BTCs in the  $K$

fields representing the MADE site aquifer, which are quite skewed ( $\widetilde{sk}_t = 3.11$ ) despite the relatively small  $\sigma_Y^2$ . This skewness value not only qualitatively agrees with the anomalous transport conditions observed at this site, it also suggests that such conditions may be mainly the effect of the low geological entropy of the aquifer. This is consistent with the presence of connected structures and organized features as suggested by several previous studies [Dogan *et al.*, 2014; Bianchi and Zheng, 2016; Zheng *et al.*, 2011 and references therein].

From Figure 8 and the comparison between skewness values from numerical simulations and corresponding predicted values (Figure S14), we can demonstrate good predictability of the developed expressions  $sk_t = f(H_R, \sigma_Y^2)$  (Equation 14) for both sets of validation data. Indeed, the large majority of estimated points fall at the expected locations in the graph, especially if we take into account the interquartile range of the distributions of the median skewness values (vertical lines). This range is particularly large for case studies considering  $K$  fields characterized by small  $H_R$  values. The error in the predictions of  $sk_t$  is generally acceptable. For instance, the calculated median value of  $sk_t$  for the scenario with  $H_R = 0.57$  and  $\sigma_Y^2 = 8.6$  (Group 2) is equal to 1.6, while the predicted value from the graph is around 1.8. For the first set of validation data, the mean absolute error is equal to 0.4. The highest discrepancy between calculated and predicted  $sk_t$  values is for the scenarios with the lowest  $H_R$  (0.76 and 0.87) for which the calculated median  $sk_t$  values are about 1.5 times smaller than corresponding predicted values. On average, the error

of validation data considering documented case studies, the errors between simulated and predicted  $sk_t$  values are in the range between about 0.2% (LLNL P48\_05) and 20% (VL aquifer). Overall, the mean percentage error of the predictions is around 10% with a tendency to underestimate the skewness.

Overall, these results prove the ability of the developed expressions (Equation 14) as a simple and sufficiently accurate predictive tool based solely on measurable aquifer properties. We argue that the predictability of our approach could be even improved in the future considering that these expressions are based on an empirical parameterization. Future research will be aimed at understanding the physical nature and mathematical derivation of the parameters in Equation 14.

## **5 Discussion: geological entropy and connectivity**

The concept of connectivity has been widely recognized as an important factor controlling flow and transport in geological media [e.g., *Fogg*, 1986; *Fogg et al.*, 2000; *Bianchi et al.*, 2011b; *Pedretti et al.*, 2013; *Molinari et al.*, 2015], and therefore several indicators have been developed with the intent to define this concept in quantitative terms. In a recent review, *Renard and Allard* [2013] classified these indicators into static indicators, measuring the probability of having connected structures in the  $K$  field, and dynamic indicators, measuring the degree of flow channeling and presence of fast preferential paths responsible for

earlier than expected particle travel times [e.g. *Knudby and Carrera*, 2005, 2006; *Willmann et al.*, 2008; *Bianchi et al.*, 2011b].

Although connectivity concepts have been the focus of multiple investigations and analyses in the last two decades, some open questions remain regarding the applicability of connectivity indicators for predictive purposes in solute transport problems. *Renard and Allard* [2013] showed for instance that static indicators do not provide values that allow a univocal ranking in terms of connectivity, and therefore the use of multiple indicators is strongly suggested. The flow and transport simulations in heterogeneous well-connected  $K$  fields presented by *Knudby and Carrera* [2005] provided evidence of a poor correlation between certain dynamic and static connectivity indicators, including the bivariate entropy index of *Journel and Deutsch* [1993]. An improved correlation have been found using static indicators based on mathematical morphology [*Tyukhova et al.*, 2015; *Tyukhova and Willmann*, 2016a]. However, these recent results have been only validated for 2-D  $K$  fields, while few studies have shown that connectivity strongly increases in 3-D field compared to 2-D fields. For instance, *Fiori and Jankovic* [2012] showed that flow channeling is significantly enhanced in 3-D fields compared to 2-D fields. The larger connectivity of 3-D systems was also used by [*Pedretti et al.*, 2013] to explain the formation of non-Fickian transport features not observed in equivalent 2-D  $K$  fields. Other studies have also shown that the emergence of non-Fickian transport features do not require fully

connected zones of relatively homogeneous high- $K$  [Bianchi *et al.*, 2011b; Fiori and Jankovic, 2012].

Although the relative entropy index  $H_R$  can be seen somewhat similar to a static connectivity indicator since in general the geological entropy of a well-connected  $K$  field is expected to be lower than a poorly connected one, there is a fundamental difference. In particular, while static connectivity indicators focus only on the spatial continuity of a specific hydrofacies or class of  $K$  values, the index  $H_R$  takes into account the spatial distribution of all the classes of  $K$  field. Therefore,  $H_R$  can be compared to a global metric that takes into account the overall structure of the  $K$  field, which is influenced by several aquifer properties (e.g., volumetric proportions of the hydrofacies or  $K$  classes), and not just by connectivity of a particular hydrofacies. We argue that geological entropy shall not be seen as an alternative to connectivity, but rather a complement to this concept since it provides a more comprehensive description of the structure of the  $K$  field. Because of the broader range of information about the spatial structure of the  $K$  field considered in the quantification of  $H_R$ , we are able to overcome some of the limitations and open issues regarding the application of connectivity indexes in transport problems, and most importantly link the structural information to the corresponding solute transport behavior in 3-D  $K$  fields.

## Conclusions

We presented a novel approach to explain solute transport behavior from the physical heterogeneity of the aquifer, here fully described by the two measurable metrics. The first ( $H_R$ ) is a new index based on information entropy concepts, which quantifies spatial disorder in the structure of  $K$  field, while the second ( $\sigma_Y^2$ ) is the log- $K$  variance of the univariate  $K$  distribution. Both metrics can be obtained from data collected during conventional hydrogeological characterization of the aquifer and from the analysis of a representative model of the spatial distribution of  $K$  classes or hydrofacies over the domain of interest. Detailed numerical simulations of conservative solute transport in several realistic scenarios of aquifer heterogeneity were used to investigate the relationships between these metrics and transport behavior, as characterized by the first three moments of the distribution of arrival times of solute particles.

Two major findings can be drawn for our numerical investigation: (1) there is a clearly identifiable dependency between transport and the degree of disorder in the  $K$  field, and (2) the Fickian or non-Fickian (i.e., “anomalous”) character of transport can be predicted solely from knowledge of the values of the two metrics  $H_R$  and  $\sigma_Y^2$ . More specifically, comparisons between results of numerical simulations in  $K$  fields with different degrees of geological entropy and  $\ln K$  variance lead to the following specific observations:

1. For scenarios considering constant  $\sigma_Y^2$  and variable  $H_R$ , the mean and the variance of the distribution of arrival times tend to increase with spatial disorder

(i.e,  $H_R$  increasing) according to power-law and logarithm functions, respectively. The distribution becomes also progressively more skewed as the structure of the  $K$  field becomes more orderly (i.e,  $H_R$  decreasing). The relationship between  $H_R$  and the skewness is best described by a power-law function. These results, which are valid for both high- $K$  and low- $K$  dominated aquifers, confirm the importance of a site specific characterization of the structure of the  $K$  field emphasized by the results of recent studies [e.g., Zech *et al.*, 2015; Bianchi and Zheng, 2016].

2. For a given degree of spatial disorder in the  $K$  field structure, the first three temporal moments of the distribution of arrival times increase with the variance  $\sigma_Y^2$ .

3. While the dependency of the variance of the arrival times is not particularly sensitive to the structure of the  $K$  field, the values of the parameters in the empirical functions describing the relationship between  $\sigma_Y^2$  and the skewness differ with respect to the degree of disorder, and therefore of  $H_R$ . This result confirms that structural information is not sufficient to fully predict all the different features of transport behavior [e.g., Ederly *et al.*, 2014; Tyukhova and Willmann, 2016b].

4. Empirical expressions relating the skewness of the BTCs to the two parameters  $H_R$  and  $\sigma_Y^2$  (Equation 14) can provide reasonable predictions of Fickian and non-Fickian transport behavior simply from knowledge of aquifer heterogeneity without fitting parameters. In recent years, the link between non-

Fickian transport features and measurable aquifer properties has been also successfully defined by *Zhang et al.* [2007, 2013, 2014]. However, while their approach is mainly applicable for aquifers systems with significant  $K$  contrasts between high- $K$  and low- $K$  sediments, we have shown that our approach is valid virtually in any combination of structure and degree of variability of the  $K$  field.

These are remarkable findings because they show that geological entropy is the fundamental aquifer property to link heterogeneity and transport behavior. Moreover, they provide motivation for future development of a new upscaled transport approach based on input transport parameters that are directly correlated to values of  $H_R$ .

A final note regards the transferability of our approach. Although in this work we focused on  $K$  fields based on stochastic distributions of hydrofacies in alluvial systems, the concept of geological entropy is applicable for predicting solute transport behavior in any conceptualization of the spatial distribution of  $K$ , regardless of the dimensionality of the domain or of the geological setting. However, the application to continuous distributions of  $K$  (e.g., multi-Gaussian representations) requires a preliminary discretization into homogenous categories, and further investigation is needed to evaluate the dependency of  $H_R$  on the criteria used for the discretization.

**Acknowledgments.** Marco Bianchi was funded by Natural Environment Research Council under the “Research Fellowship Programme” of the British

Accepted ms, *Water Resources Research* (2017), doi: 10.1002/2016WR020195

Geological Survey. Marco Bianchi publishes with the permission of the Executive Director of the British Geological Survey. We are grateful to Graham Fogg and two anonymous reviewers for their constructive comments during the revision process. Synthetic data and the code to calculate geological entropy are available upon request. Data for the case studies can be found in the list of references in Table 2.

## References

- Allen-King, R. M., R. M. Halket, D. R. Gaylord, and M. J. L. Robin (1998), Characterizing the heterogeneity and correlation of perchloroethene sorption and hydraulic conductivity using a facies-based approach, *Water Resour. Res.*, *34*(3), 385–396, doi:10.1029/97WR03496.
- Anderson, M. P. (1989), Hydrogeologic facies models to delineate large-scale spatial trends in glacial and glaciofluvial sediments, *Geological Society of America Bulletin*, *101*(4), 501–511, doi:10.1130/0016-7606(1989)101<0501:HFMTDL>2.3.CO;2.
- Bakshvskaya, V. A., and S. P. Pozdniakov (2015), Simulation of Hydraulic Heterogeneity and Upscaling Permeability and Dispersivity in Sandy-Clay Formations, *Math Geosci*, *48*(1), 45–64, doi:10.1007/s11004-015-9590-1.
- Barba, J., H. Jeanty, P. Fenster, and J. Gil (1989), The use of local entropy measures in edge detection for cytological image analysis, *J Microsc*, *156*(Pt 1), 125–134.
- Batty, M., R. Morphet, P. Masucci, and K. Stanilov (2014), Entropy, complexity, and spatial information, *Journal of Geographical Systems*, *16*(4), 363–385, doi:10.1007/s10109-014-0202-2.
- Beretta, G. P., and J. Terrenghi (2016), Groundwater flow in the Venice lagoon and remediation of the Porto Marghera industrial area (Italy), *Hydrogeol J*, 1–15, doi:10.1007/s10040-016-1517-5.
- Bianchi, M., and C. Zheng (2016), A lithofacies approach for modeling non-Fickian solute transport in a heterogeneous alluvial aquifer, *Water Resour. Res.*, *52*(1), 552–565, doi:10.1002/2015WR018186.
- Bianchi, M., C. Zheng, G. R. Tick, and S. M. Gorelick (2011a), Investigation of Small-Scale Preferential Flow with a Forced-Gradient Tracer Test, *Ground Water*, *49*(4), 503–514, doi:10.1111/j.1745-6584.2010.00746.x.
- Bianchi, M., C. Zheng, C. Wilson, G. R. Tick, G. Liu, and S. M. Gorelick (2011b), Spatial connectivity in a highly heterogeneous aquifer: From cores to preferential flow paths, *Water Resources Research*, *47*(5), doi:10.1029/2009WR008966.
- Bianchi, M., T. Kearsy, and A. Kingdon (2015), Integrating deterministic lithostratigraphic models in stochastic realizations of subsurface heterogeneity. Impact on predictions of lithology, hydraulic heads and

- groundwater fluxes, *Journal of Hydrology*, 531, 557–573, doi:10.1016/j.jhydrol.2015.10.072.
- Boggs, J. M., S. C. Young, L. M. Beard, L. W. Gelhar, K. R. Rehfeldt, and E. E. Adams (1992), Field study of dispersion in a heterogeneous aquifer: 1. Overview and site description, *Water Resour. Res.*, 28(12), 3281–3291, doi:10.1029/92WR01756.
- Carle, S. F. (1999), T-PROGS: Transition probability geostatistical software, *University of California, Davis, CA*, 84.
- Carle, S. F., and G. E. Fogg (1996), Transition probability-based indicator geostatistics, *Mathematical geology*, 28(4), 453–476.
- Carle, S. F., and G. E. Fogg (1997), Modeling spatial variability with one and multidimensional continuous-lag Markov chains, *Mathematical Geology*, 29(7), 891–918.
- Castillo, A., F. Castelli, and D. Entekhabi (2015), An entropy-based measure of hydrologic complexity and its applications, *Water Resour. Res.*, 51(7), 5145–5160, doi:10.1002/2014WR016035.
- Cherubini, C., C. I. Giasi, and N. Pastore (2013), Evidence of non-Darcy flow and non-Fickian transport in fractured media at laboratory scale, *Hydrol. Earth Syst. Sci.*, 17(7), 2599–2611, doi:10.5194/hess-17-2599-2013.
- Chiogna, G., D. L. Hochstetler, A. Bellin, P. K. Kitanidis, and M. Rolle (2012), Mixing, entropy and reactive solute transport, *Geophys. Res. Lett.*, 39(20), L20405, doi:10.1029/2012GL053295.
- Christakos, G. (1990), A Bayesian/maximum-entropy view to the spatial estimation problem, *Math Geol*, 22(7), 763–777, doi:10.1007/BF00890661.
- Dagan, G. (1984), Solute transport in heterogeneous porous formations, *Journal of Fluid Mechanics*, 145, 151–177, doi:10.1017/S0022112084002858.
- Dagan, G. (1989), *Flow and Transport in Porous Formations*, Springer Berlin Heidelberg, Berlin, Heidelberg.
- Dagan, G., and S. P. Neuman (2005), *Subsurface Flow and Transport: A Stochastic Approach*, Cambridge University Press.
- Deutsch, C. V., and A. G. Journel (1998), *GSLIB: Geostatistical Software Library and User's Guide*, Oxford University Press.

- Dogan, M., R. L. Van Dam, G. Liu, M. M. Meerschaert, J. J. Butler, G. C. Bohling, D. A. Benson, and D. W. Hyndman (2014), Predicting flow and transport in highly heterogeneous alluvial aquifers, *Geophys. Res. Lett.*, *41*(21), 2014GL061800, doi:10.1002/2014GL061800.
- Ederly, Y., A. Guadagnini, H. Scher, and B. Berkowitz (2014), Origins of anomalous transport in heterogeneous media: Structural and dynamic controls, *Water Resour. Res.*, *50*(2), 1490–1505, doi:10.1002/2013WR015111.
- Elfeki, A. M. M., and F. M. Dekking (2005), Modelling Subsurface Heterogeneity by Coupled Markov Chains: Directional Dependency, Walther's Law and Entropy, *Geotechnical and Geological Engineering*, *23*(6), 721–756, doi:10.1007/s10706-004-2899-z.
- Engdahl, N. B., T. R. Ginn, and G. E. Fogg (2013), Using groundwater age distributions to estimate the effective parameters of Fickian and non-Fickian models of solute transport, *Advances in Water Resources*, *54*, 11–21, doi:10.1016/j.advwatres.2012.12.008.
- Fernández-García, D., T. H. Illangasekare, and H. Rajaram (2005), Differences in the scale dependence of dispersivity and retardation factors estimated from forced-gradient and uniform flow tracer tests in three-dimensional physically and chemically heterogeneous porous media, *Water Resources Research*, *41*(3), n/a-n/a, doi:10.1029/2004WR003125.
- Fiori, A., and I. Jankovic (2012), On Preferential Flow, Channeling and Connectivity in Heterogeneous Porous Formations, *Mathematical Geosciences*, *44*(2), 133–145, doi:10.1007/s11004-011-9365-2.
- Fiori, A., F. Boso, F. P. J. de Barros, S. De Bartolo, A. Frampton, G. Severino, S. Suweis, and G. Dagan (2010), An indirect assessment on the impact of connectivity of conductivity classes upon longitudinal asymptotic macrodispersivity, *Water Resour. Res.*, *46*(8), W08601, doi:10.1029/2009WR008590.
- Flach, G. P. (2012), Relationship Between Dual-Domain Parameters and Practical Characterization Data, *Ground Water*, *50*(2), 216–229, doi:10.1111/j.1745-6584.2011.00834.x.
- Fogg, G. E. (1986), Groundwater Flow and Sand Body Interconnectedness in a Thick, Multiple-Aquifer System, *Water Resour. Res.*, *22*(5), 679–694, doi:10.1029/WR022i005p00679.

- Fogg, G. E., C. D. Noyes, and S. F. Carle (1998), Geologically based model of heterogeneous hydraulic conductivity in an alluvial setting, *Hydrogeology Journal*, 6(1), 131–143, doi:10.1007/s100400050139.
- Fogg, G. E., S. F. Carle, and C. Green (2000), Connected-network paradigm for the alluvial aquifer system, *Geological Society of America Special Papers*, 348, 25–42, doi:10.1130/0-8137-2348-5.25.
- Gelhar, L. W. (1993), *Stochastic Subsurface Hydrology*, Prentice-Hall.
- Gelhar, L. W., and C. L. Axness (1983), Three-dimensional stochastic analysis of macrodispersion in aquifers, *Water Resour. Res.*, 19(1), 161–180, doi:10.1029/WR019i001p00161.
- Gómez-Hernández, J. J., and X.-H. Wen (1998), To be or not to be multi-Gaussian? A reflection on stochastic hydrogeology, *Advances in Water Resources*, 21(1), 47–61, doi:10.1016/S0309-1708(96)00031-0.
- Gotovac, H., V. Cvetkovic, and R. Andricevic (2010), Significance of higher moments for complete characterization of the travel time probability density function in heterogeneous porous media using the maximum entropy principle, *Water Resour. Res.*, 46(5), W05502, doi:10.1029/2009WR008220.
- Harbaugh, A. W. (2005), *MODFLOW-2005, The U.S. Geological Survey modular ground-water model—the Ground-Water Flow Process*, U.S. Geological Survey Techniques and Methods, U.S. Geological Survey.
- Harter, T. (2005), Finite-size scaling analysis of percolation in three-dimensional correlated binary Markov chain random fields, *Physical Review E*, 72(2), doi:10.1103/PhysRevE.72.026120.
- Huang, L., R. W. Ritzi, and R. Ramanathan (2012), Conservative Models: Parametric Entropy vs. Temporal Entropy in Outcomes, *Ground Water*, 50(2), 199–206, doi:10.1111/j.1745-6584.2011.00832.x.
- Jaynes, E. T. (1957), Information Theory and Statistical Mechanics, *Phys. Rev.*, 106(4), 620–630, doi:10.1103/PhysRev.106.620.
- Journel, A. G., and C. V. Deutsch (1993), Entropy and spatial disorder, *Mathematical Geology*, 25(3), 329–355.
- Kitanidis, P. K. (1994), The concept of the Dilution Index, *Water Resour. Res.*, 30(7), 2011–2026, doi:10.1029/94WR00762.

- Klise, K. A., G. S. Weissmann, S. A. McKenna, E. M. Nichols, J. D. Frechette, T. F. Wawrzyniec, and V. C. Tidwell (2009), Exploring solute transport and streamline connectivity using lidar-based outcrop images and geostatistical representations of heterogeneity, *Water Resour. Res.*, 45(5), W05413, doi:10.1029/2008WR007500.
- Knudby, C., and J. Carrera (2005), On the relationship between indicators of geostatistical, flow and transport connectivity, *Advances in Water Resources*, 28(4), 405–421, doi:10.1016/j.advwatres.2004.09.001.
- Knudby, C., and J. Carrera (2006), On the use of apparent hydraulic diffusivity as an indicator of connectivity, *Journal of Hydrology*, 329(3–4), 377–389, doi:10.1016/j.jhydrol.2006.02.026.
- LaBolle, E. M., and G. E. Fogg (2001), Role of Molecular Diffusion in Contaminant Migration and Recovery in an Alluvial Aquifer System, *Transport in Porous Media*, 42(1–2), 155–179, doi:10.1023/A:1006772716244.
- Lee, S.-Y., S. F. Carle, and G. E. Fogg (2007), Geologic heterogeneity and a comparison of two geostatistical models: Sequential Gaussian and transition probability-based geostatistical simulation, *Advances in Water Resources*, 30(9), 1914–1932, doi:10.1016/j.advwatres.2007.03.005.
- Leibovici, D. G., C. Claramunt, D. Le Guyader, and D. Brosset (2014), Local and global spatio-temporal entropy indices based on distance-ratios and co-occurrences distributions, *International Journal of Geographical Information Science*, 28(5), 1061–1084, doi:10.1080/13658816.2013.871284.
- Liu, G., C. Zheng, and S. M. Gorelick (2004), Limits of applicability of the advection-dispersion model in aquifers containing connected high-conductivity channels, *Water Resour. Res.*, 40(8), W08308, doi:10.1029/2003WR002735.
- Martina, M. L. V., and D. Entekhabi (2006), Identification of runoff generation spatial distribution using conventional hydrologic gauge time series, *Water Resour. Res.*, 42(8), W08431, doi:10.1029/2005WR004783.
- Mays, D. C., B. A. Faybishenko, and S. Finsterle (2002), Information entropy to measure temporal and spatial complexity of unsaturated flow in heterogeneous media, *Water Resources Research*, 38(12), 49-1-49–11, doi:10.1029/2001WR001185.

Accepted ms, *Water Resources Research* (2017), doi: 10.1002/2016WR020195

Miall, A. (2014), *Fluvial Depositional Systems*, Springer International Publishing, Cham.

Molinari, A., D. Pedretti, and C. Fallico (2015), Analysis of convergent flow tracer tests in a heterogeneous sandy box with connected gravel channels, *Water Resour. Res.*, 51(7), 5640–5657, doi:10.1002/2014WR016216.

Neuman, S. P., and D. M. Tartakovsky (2009), Perspective on theories of non-Fickian transport in heterogeneous media, *Advances in Water Resources*, 32(5), 670–680, doi:10.1016/j.advwatres.2008.08.005.

Ottino, J. M. (1990), Mixing, Chaotic Advection, and Turbulence, *Annual Review of Fluid Mechanics*, 22(1), 207–254, doi:10.1146/annurev.fl.22.010190.001231.

Pedretti, D., and D. Fernández-García (2013), An automatic locally-adaptive method to estimate heavily-tailed breakthrough curves from particle distributions, *Advances in Water Resources*, 59, 52–65, doi:10.1016/j.advwatres.2013.05.006.

Pedretti, D., D. Fernández-García, D. Bolster, and X. Sanchez-Vila (2013), On the formation of breakthrough curves tailing during convergent flow tracer tests in three-dimensional heterogeneous aquifers, *Water Resour. Res.*, 49(7), 4157–4173, doi:10.1002/wrcr.20330.

Pedretti, D., A. Molinari, C. Fallico, and S. Guzzi (2016), Implications of the change in confinement status of a heterogeneous aquifer for scale-dependent dispersion and mass-transfer processes, *Journal of Contaminant Hydrology*, 193, 86–95, doi:10.1016/j.jconhyd.2016.09.005.

Renard, P., and D. Allard (2013), Connectivity metrics for subsurface flow and transport, *Advances in Water Resources*, 51, 168–196, doi:10.1016/j.advwatres.2011.12.001.

Renard, P., and G. de Marsily (1997), Calculating equivalent permeability: a review, *Advances in Water Resources*, 20(5–6), 253–278, doi:10.1016/S0309-1708(96)00050-4.

Riva, M., A. Guadagnini, D. Fernandez-Garcia, X. Sanchez-Vila, and T. Ptak (2008), Relative importance of geostatistical and transport models in describing heavily tailed breakthrough curves at the Lauswiesen site, *Journal of Contaminant Hydrology*, 101(1–4), 1–13, doi:10.1016/j.jconhyd.2008.07.004.

Accepted ms, *Water Resources Research* (2017), doi: 10.1002/2016WR020195

Ronayne, M. J., S. M. Gorelick, and C. Zheng (2010), Geological modeling of submeter scale heterogeneity and its influence on tracer transport in a fluvial aquifer, *Water Resources Research*, 46(10), doi:10.1029/2010WR009348.

Rubin, Y. (2003), *Applied Stochastic Hydrogeology*, Oxford University Press.

Salamon, P., D. Fernández-García, and J. J. Gómez-Hernández (2006), Modeling mass transfer processes using random walk particle tracking, *Water Resour. Res.*, 42(11), W11417, doi:10.1029/2006WR004927.

Sanchez-Vila, X., A. Guadagnini, and J. Carrera (2006), Representative hydraulic conductivities in saturated groundwater flow, *Reviews of Geophysics*, 44(3), doi:10.1029/2005RG000169.

Shannon, C. E. (1948), A Mathematical Theory of Communication, *Bell System Technical Journal*, 27(3), 379–423, doi:10.1002/j.1538-7305.1948.tb01338.x.

Shapiro, A. M., and V. D. Cvetkovic (1988), Stochastic analysis of solute arrival time in heterogeneous porous media, *Water Resour. Res.*, 24(10), 1711–1718, doi:10.1029/WR024i010p01711.

Siirila-Woodburn, E. R., and R. M. Maxwell (2015), A heterogeneity model comparison of highly resolved statistically anisotropic aquifers, *Advances in Water Resources*, 75, 53–66, doi:10.1016/j.advwatres.2014.10.011.

Singh, V. P. (2011), Hydrologic Synthesis Using Entropy Theory: Review, *Journal of Hydrologic Engineering*, 16(5), 421–433, doi:10.1061/(ASCE)HE.1943-5584.0000332.

Stauffer, D., and A. Aharony (1994), *Introduction To Percolation Theory*, CRC Press.

Swanson, R. D., A. Binley, K. Keating, S. France, G. Osterman, F. D. Day-Lewis, and K. Singha (2015), Anomalous solute transport in saturated porous media: Relating transport model parameters to electrical and nuclear magnetic resonance properties, *Water Resour. Res.*, 51(2), 1264–1283, doi:10.1002/2014WR015284.

Teles, V., F. Delay, and G. de Marsily (2004), Comparison of genesis and geostatistical methods for characterizing the heterogeneity of alluvial media: Groundwater flow and transport simulations, *Journal of Hydrology*, 294(1–3), 103–121, doi:10.1016/j.jhydrol.2003.11.041.

- Terrenghi, J., M. Bianchi, and G. P. Beretta (2016), Should we collect more K data or more aquifer samples for effective subsurface characterization? A comparative study based on reproducibility of flow and transport modelling results, in *Proceedings of the 43rd IAH Congress*, vol. 2331, Montpellier, France.
- Tyukhova, A. R., and M. Willmann (2016a), Connectivity metrics based on the path of smallest resistance, *Advances in Water Resources*, 88, 14–20, doi:10.1016/j.advwatres.2015.11.014.
- Tyukhova, A. R., and M. Willmann (2016b), Conservative transport upscaling based on information of connectivity, *Water Resources Research*, 52(9), 6867–6880, doi:10.1002/2015WR018331.
- Tyukhova, A. R., W. Kinzelbach, and M. Willmann (2015), Delineation of connectivity structures in 2-D heterogeneous hydraulic conductivity fields, *Water Resour. Res.*, 51(7), 5846–5854, doi:10.1002/2014WR015283.
- Vassena, C., L. Cattaneo, and M. Giudici (2009), Assessment of the role of facies heterogeneity at the fine scale by numerical transport experiments and connectivity indicators, *Hydrogeol J*, 18(3), 651–668, doi:10.1007/s10040-009-0523-2.
- Vranken, I., J. Baudry, M. Aubinet, M. Visser, and J. Bogaert (2015), A review on the use of entropy in landscape ecology: heterogeneity, unpredictability, scale dependence and their links with thermodynamics, *Landscape Ecology*, 30(1), 51–65, doi:10.1007/s10980-014-0105-0.
- Weissmann, G. S., S. F. Carle, and G. E. Fogg (1999), Three-dimensional hydrofacies modeling based on soil surveys and transition probability geostatistics, *Water Resour. Res.*, 35(6), 1761–1770, doi:10.1029/1999WR900048.
- Wellmann, J. F., and K. Regenauer-Lieb (2012), Uncertainties have a meaning: Information entropy as a quality measure for 3-D geological models, *Tectonophysics*, 526–529, 207–216, doi:10.1016/j.tecto.2011.05.001.
- Wen, X.-H., and J. J. Gómez-Hernández (1998), Numerical modeling of macrodispersion in heterogeneous media: a comparison of multi-Gaussian and non-multi-Gaussian models, *Journal of Contaminant Hydrology*, 30(1–2), 129–156, doi:10.1016/S0169-7722(97)00035-1.
- Willmann, M., J. Carrera, and X. Sánchez-Vila (2008), Transport upscaling in heterogeneous aquifers: What physical parameters control memory

- functions?, *Water Resour. Res.*, 44(12), W12437, doi:10.1029/2007WR006531.
- Woodbury, A. D., and T. J. Ulrych (1993), Minimum relative entropy: Forward probabilistic modeling, *Water Resour. Res.*, 29(8), 2847–2860, doi:10.1029/93WR00923.
- Wu, Y., Y. Zhou, G. Saveriades, S. Agaian, J. P. Noonan, and P. Natarajan (2013), Local Shannon entropy measure with statistical tests for image randomness, *Information Sciences*, 222, 323–342, doi:10.1016/j.ins.2012.07.049.
- Zech, A., S. Attinger, V. Cvetkovic, G. Dagan, P. Dietrich, A. Fiori, Y. Rubin, and G. Teutsch (2015), Is unique scaling of aquifer macrodispersivity supported by field data?, *Water Resour. Res.*, 51(9), 7662–7679, doi:10.1002/2015WR017220.
- Zhang, Y., D. A. Benson, and B. Baeumer (2007), Predicting the Tails of Breakthrough Curves in Regional-Scale Alluvial Systems, *Ground Water*, 45(4), 473–484, doi:10.1111/j.1745-6584.2007.00320.x.
- Zhang, Y., C. T. Green, and G. E. Fogg (2013), The impact of medium architecture of alluvial settings on non-Fickian transport, *Advances in Water Resources*, 54, 78–99, doi:10.1016/j.advwatres.2013.01.004.
- Zhang, Y., C. T. Green, and B. Baeumer (2014), Linking aquifer spatial properties and non-Fickian transport in mobile–immobile like alluvial settings, *Journal of Hydrology*, 512, 315–331, doi:10.1016/j.jhydrol.2014.02.064.
- Zheng, C., and S. M. Gorelick (2003), Analysis of Solute Transport in Flow Fields Influenced by Preferential Flowpaths at the Decimeter Scale, *Ground Water*, 41(2), 142–155, doi:10.1111/j.1745-6584.2003.tb02578.x.
- Zheng, C., M. Bianchi, and S. M. Gorelick (2011), Lessons Learned from 25 Years of Research at the MADE Site, *Ground Water*, 49(5), 649–662, doi:10.1111/j.1745-6584.2010.00753.x.
- Zhu, L., Z. Dai, H. Gong, C. Gable, and P. Teatini (2015), Statistic inversion of multi-zone transition probability models for aquifer characterization in alluvial fans, *Stoch Environ Res Risk Assess*, 30(3), 1005–1016, doi:10.1007/s00477-015-1089-2.
- Zinn, B., and C. F. Harvey (2003), When good statistical models of aquifer heterogeneity go bad: A comparison of flow, dispersion, and mass transfer

in connected and multivariate Gaussian hydraulic conductivity fields, *Water Resour. Res.*, 39(3), 1051, doi:10.1029/2001WR001146.

Table 1. Summary of the parameters for the considered scenarios of aquifer heterogeneity.  $p$  represents the volumetric proportion of a hydrofacies within the considered domain. Subscripts “HK”, “IK”, and “LK” indicate three hydrofacies with high, intermediate and low conductivity, respectively.  $L_h$  and  $L_z$  indicate the mean length [m] of the facies in the horizontal plan and in the vertical direction, respectively.  $K_i$  is the hydraulic conductivity for the facies “i”.  $\sigma_Y^2$  is the variance of the log-transformed  $K$  values with  $Y = \ln(K)$ .  $H_G$  is the global entropy and  $H_R$  is relative entropy index. For each group, one or more properties are varied as graphically described in Figure 3.

Group	Volumetric fractions			Mean lengths		K		Heterogeneity parameters		
	$p_{HK}$	$p_{IK}$	$p_{LK}$	$L_h$	$L_z$	$K_{HK}/K_{IK}$	$K_{HK}/K_{LK}$	$\sigma_Y^2$	$H_G$	$H_R$
1	0.20	0.20	0.60	Figure 3a	1	$10^2$	$10^3$	7.3	0.950	Figure 3a
2	0.60	0.20	0.20	Figure 3a	1	$10^2$	$10^3$	8.6	0.950	Figure 3a
3	0.33	0.33	0.33	2.5	1	10	Figure 3b	Figure 3b	1.099	0.676
4	0.33	0.33	0.33	7.5	1	10	Figure 3b	Figure 3b	1.099	0.385
5	0.33	0.33	0.33	20	2	10	Figure 3b	Figure 3b	1.099	0.288

6	0.33	Figure 3c	Figure 3c	15	1	$10^2$	$10^3$	Figure 3c	Figure 3c	Figure 3c
---	------	--------------	--------------	----	---	--------	--------	--------------	--------------	--------------

Table 2. Summary of parameters and calculated values for the documented case studies.

Aquifer type	Description	$H_G$	$H_R$	$\sigma_Y^2$	$\widetilde{sk}_t$	Bibliographic reference
MADE	Five hydrofacies with relatively small $K$ contrasts resulting in a binomial $K$ distribution	1.53	0.36	3.35	3.11	Bianchi and Zheng [2016]
VL	Three lithofacies with comparable proportions (sand, clay, silt) and significant $K$ contrasts	1.09	0.52	$\frac{15.0}{2}$	5.20	Terrenghi et al. [2016]
LLNL P18	Four hydrofacies with significant $K$ contrasts. Predominance of the low $K$ hydrofacies (56%)	1.14	0.32	$\frac{24.9}{0}$	12.47	Fogg et al. [1998] Labolle and Fogg [2001] Zhang et al. [2013]
LLNL P48	Four hydrofacies with significant $K$ contrasts. Predominance of the high $K$ hydrofacies (48%)	1.20	0.42	$\frac{23.3}{0}$	7.01	Zhang et al. [2013]
LLNL P48_05	Similar to P48, but shorter mean lengths of the hydrofacies	1.20	0.74	$\frac{23.3}{0}$	2.64	Zhang et al. [2013]

## Disorderly system

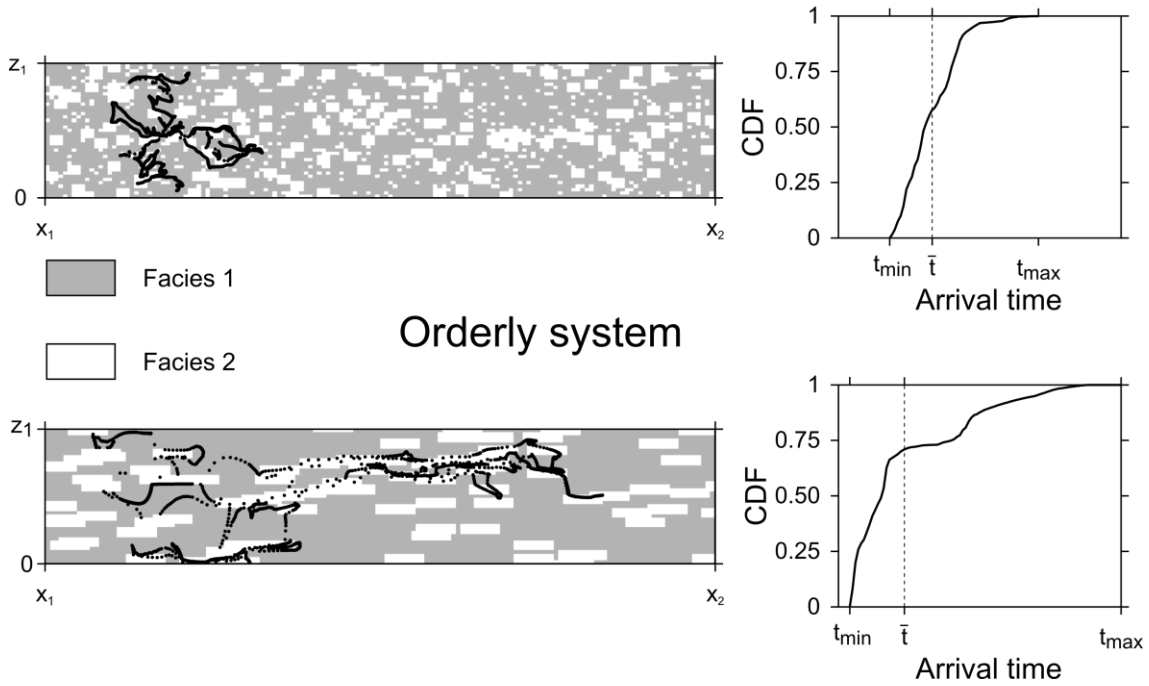


Figure 1. Solute transport in two binary systems characterized by different degrees of spatial disorder. Snapshots of particle locations in the two systems (left) are shown for the same time after injection. Cumulative density functions (CDF) of the arrival times are shown on the right.  $t_{min}$  is the arrival time of the fastest particle.  $t_{max}$  is the arrival time of the slowest particle.  $\bar{t}$  is the mean arrival time.

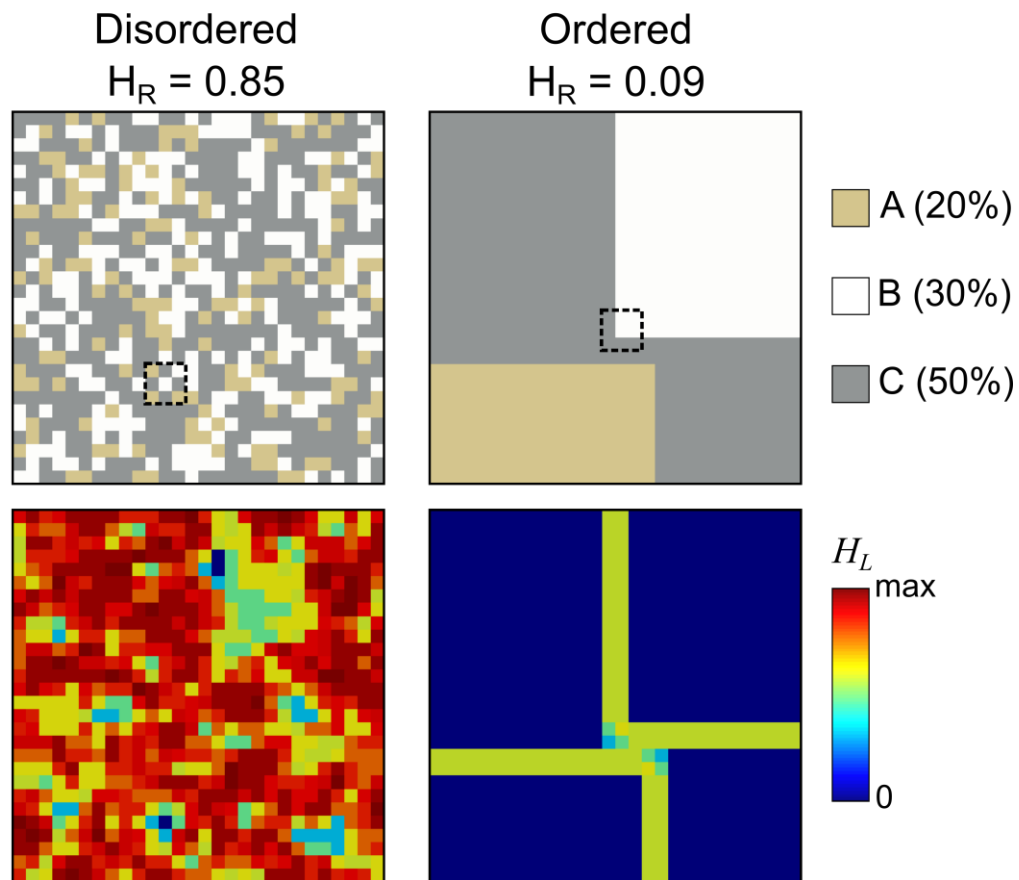


Figure 2. Local and relative entropy calculation for disorderly (left) and orderly (right) systems consisting of three categories A, B, and C and global entropy  $H_G$  equal to 1.030. Dashed rectangles indicate an example of subsets of 9 adjacent cells used to calculate the local entropy  $H_L$ . For the disorderly system the marginal probabilities of the categories within the area indicated by the dashed rectangle are equal to  $2/9$  (A),  $3/9$  (B), and  $4/9$  (C) corresponding to a  $H_L$  value of 1.061. This is very close to maximum value, which is equal to  $\ln(3) = 1.099$ . On the other hand, for the orderly system, the marginal probabilities of the categories

Accepted ms, Water Resources Research (2017), doi: 10.1002/2016WR020195

within the rectangle are equal to  $0/9$  (A),  $4/9$  (B), and  $5/9$  (C) corresponding to a  $H_L$  value of 0.687.

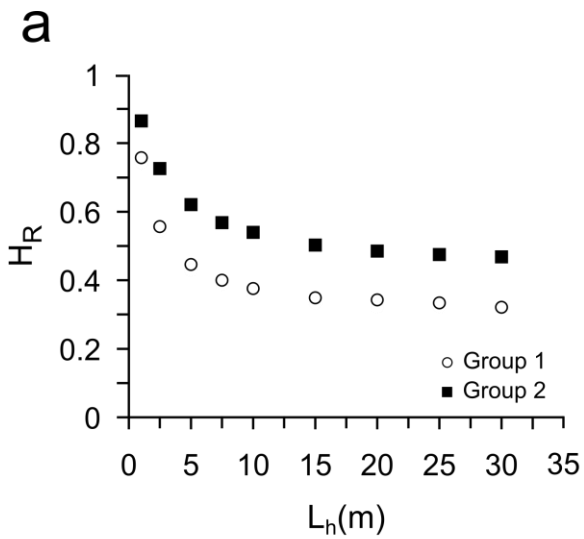
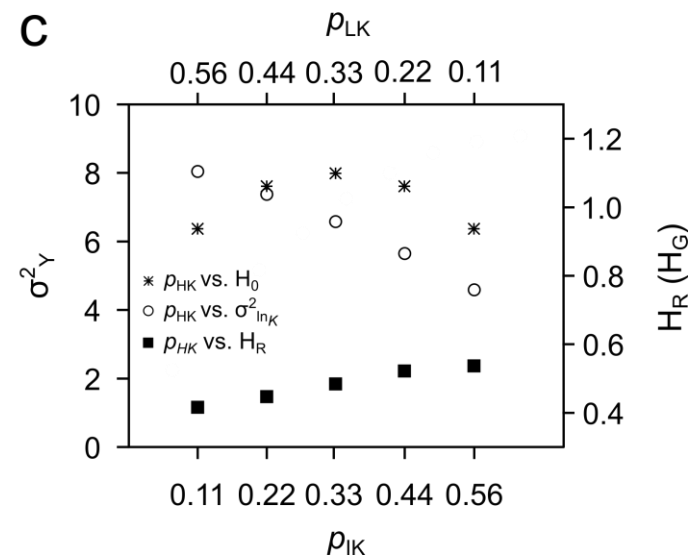
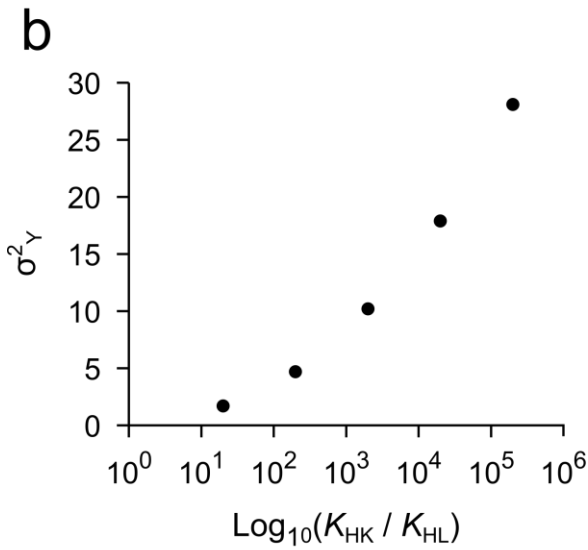


Figure 3. Descriptive parameters for the groups of scenarios of aquifer heterogeneity. (a) Variation of  $H_R$  with  $L_h$  in Groups 1-2. (b) Variation of  $\sigma_Y^2$  with  $K$  contrast ( $K_{HK}/K_{LK}$ ) in Groups 3-5. (c) Variations of  $H_G$ ,  $H_R$  and  $\sigma_Y^2$  with volumetric proportion of hydrofacies IK ( $p_{IK}$ ) and LK ( $p_{LK}$ ) in Group 6.



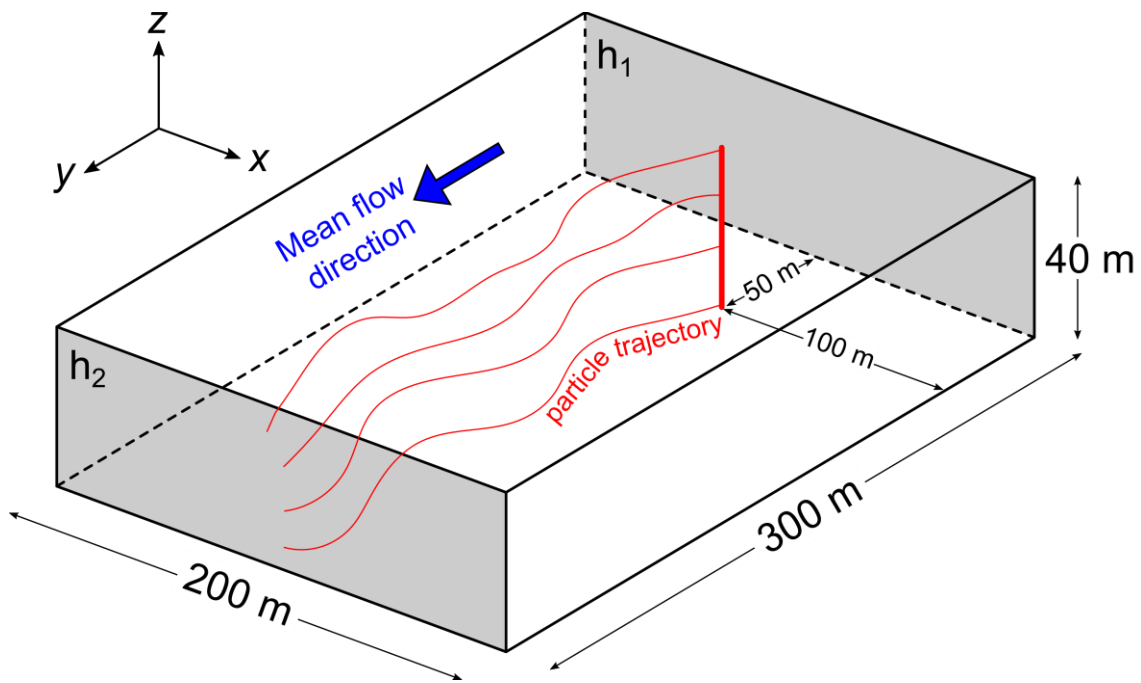


Figure 4. Numerical model setup. Specified hydraulic heads ( $h_1$  and  $h_2$ ) boundary conditions are applied at the grey-shaded sides. Particles are injected along the vertical line shown in red and exit the domain at the outflow boundary with head =  $h_2$ .

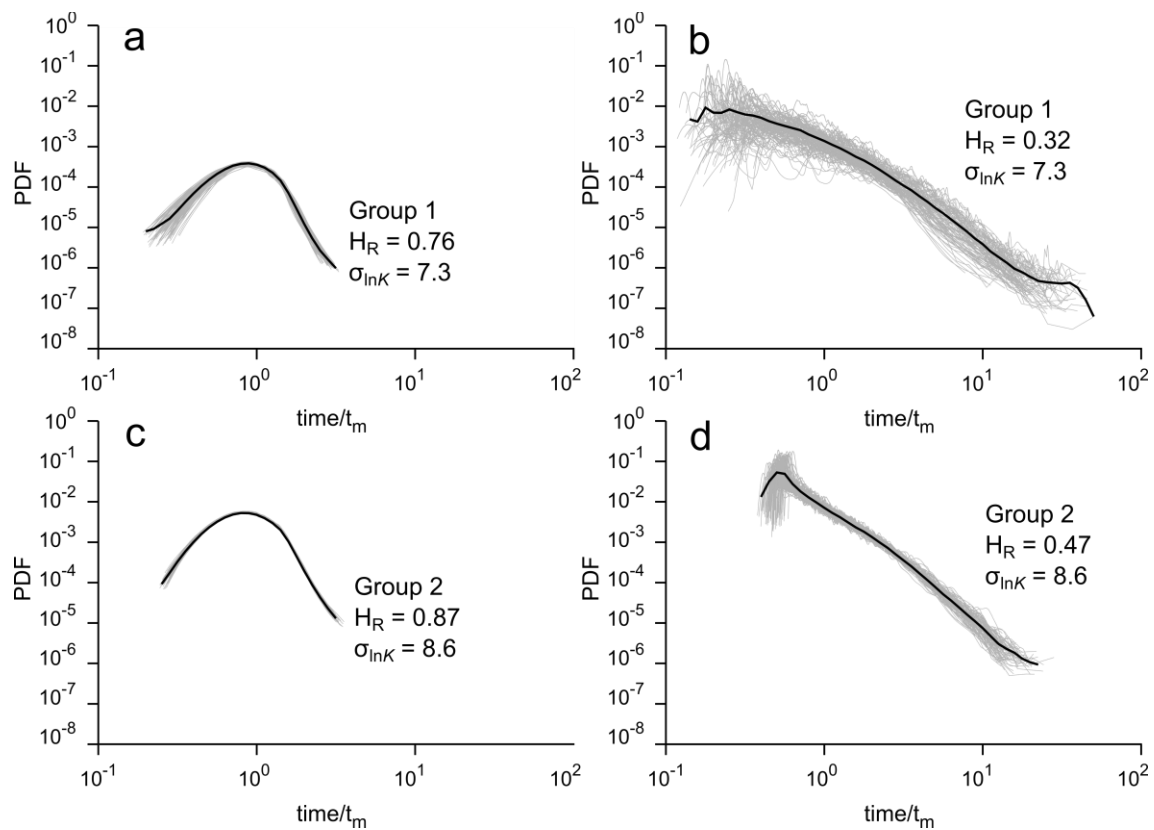


Figure 5. Ensemble of one hundred arrival time probability density functions (PDFs) for two scenarios of Groups 1 (a,b) and 2 (c,d). Grey curves represent individual realizations. Black curves indicate ensemble means.

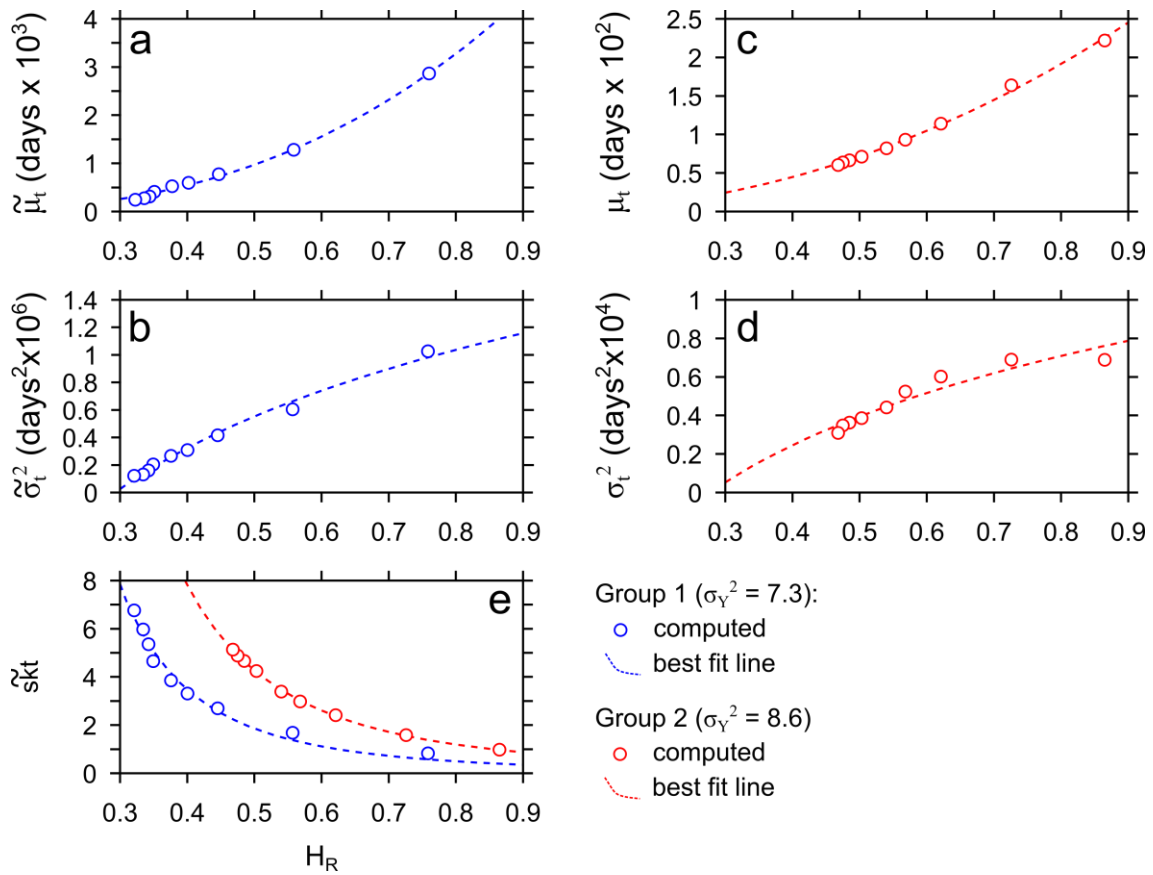


Figure 6. Median values of the moments of the BTCs for Group 1 and 2.  $R^2$  values for the best fitted lines are: 0.996 (a), 0.989 (b), 0.997 (c), 0.913 (d), 0.980 (e, Group 1), and 0.999 (e, Group 2).

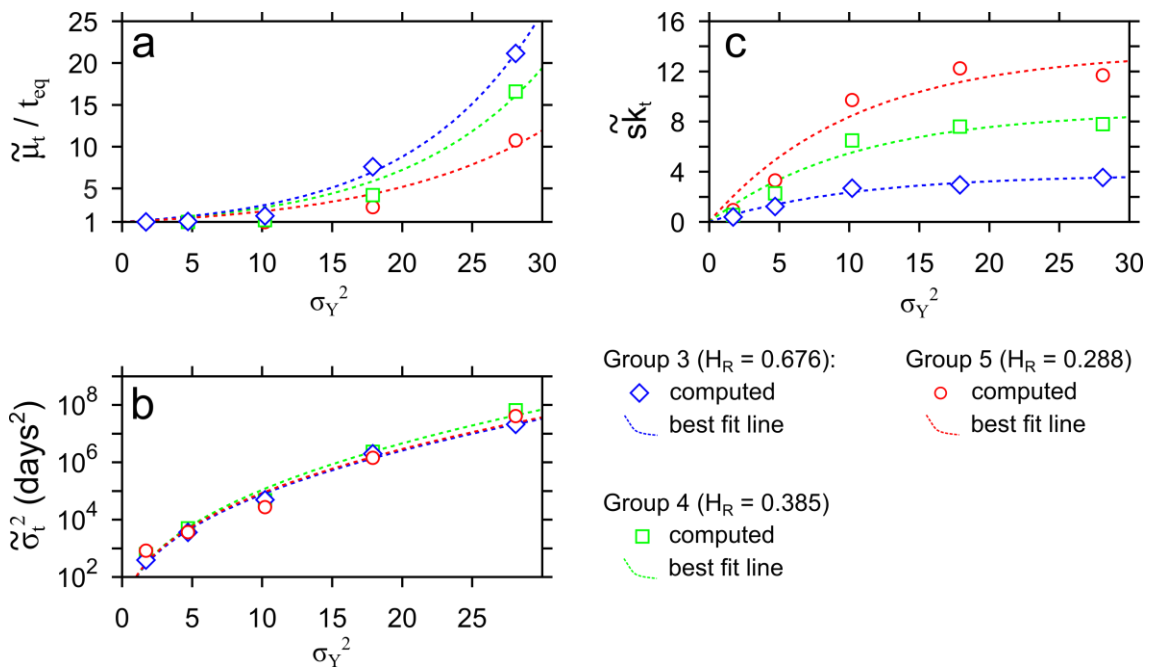


Figure 7. Median values of the moments of the BTCs for Groups 3 – 5.  $R^2$  values for the best fitted lines are in the range 0.987 – 0.992 (a), 0.963 – 0.993 (b), and 0.929 – 0.975 (c).

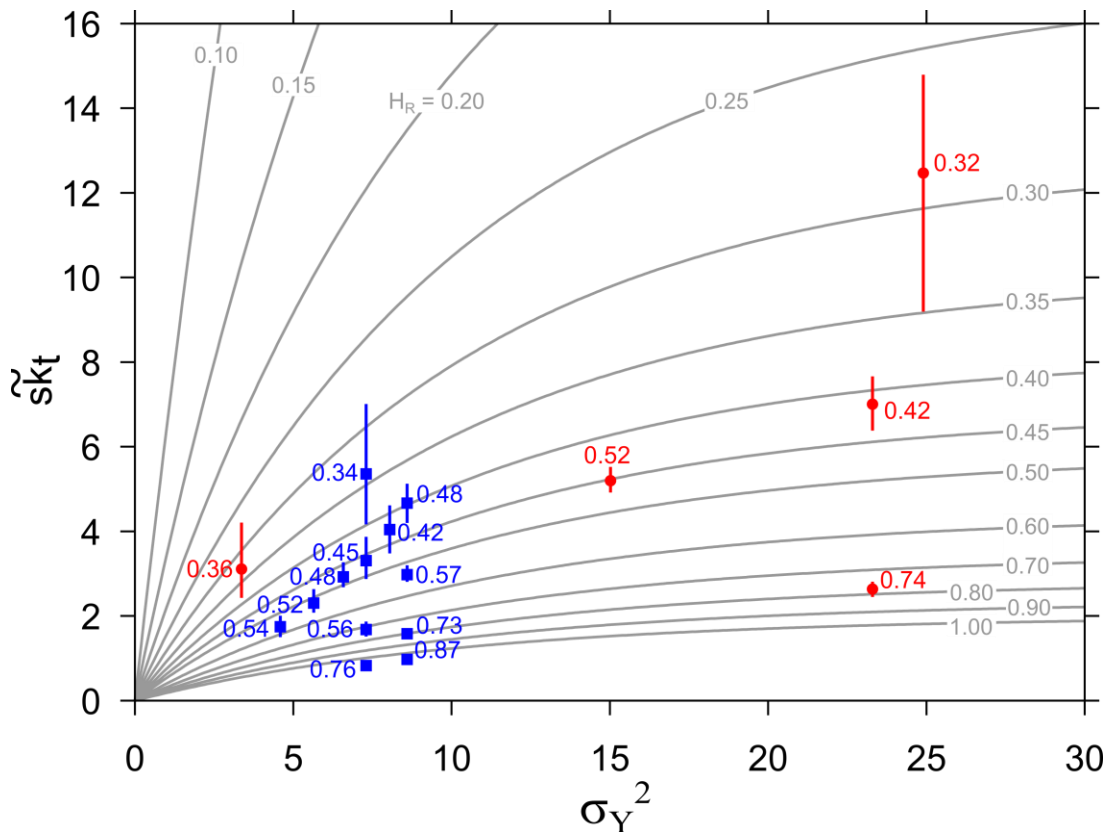


Figure 8. Curves  $s_{k_t} = f(H_R, \sigma_Y^2)$  for different  $\sigma_Y^2$  and  $H_R$  values (Equation 12).

Validation data based on transport simulations from Groups 1, 2 and 6 are plotted in blue. Data from documented case studies are plotted in red. Vertical lines indicate the interquantile range of the distributions of simulated skewness values. See text for details.



*Water Resources Research*

Supporting Information for

**Geological entropy and solute transport in heterogeneous porous media**

Marco Bianchi<sup>1</sup> and Daniele Pedretti<sup>2</sup>

<sup>1</sup> British Geological Survey, Environmental Science Centre, Keyworth, Nottingham, United Kingdom.

<sup>2</sup> Geological Survey of Finland (GTK), Espoo, Finland.

**Contents of this file**

Text S1

Figures S1 to S15

**Introduction**

The supporting information consists of additional text and fifteen figures.

**Figure S1** shows variations of the average of the local entropy ( $H_L$ ) with respect to the length ( $l$ ) of the subdomain considered for the calculation.

**Figures S2-S5** show examples of generated hydrofacies distributions for each group of scenarios, as well as corresponding maps of the spatial distribution of local entropy  $H_L$ .

Ensemble BTCs for five selected scenarios in each group are presented in **Figures S6-S9**.

**Figures S10-S12** show boxplots of the distributions of temporal moments of the BTCs for selected scenarios of each group.

**Figure S13** shows the empirical correlation between  $H_R$  and the parameter  $\alpha$  of Equation 12 in the paper.

**Figure S14** compares the simulated and empirical skewness values shown in Figure 8 of the paper.

The results of transport simulations in the scenarios of Group 6 are presented and discussed in **Text S1** and **Figure S15**.

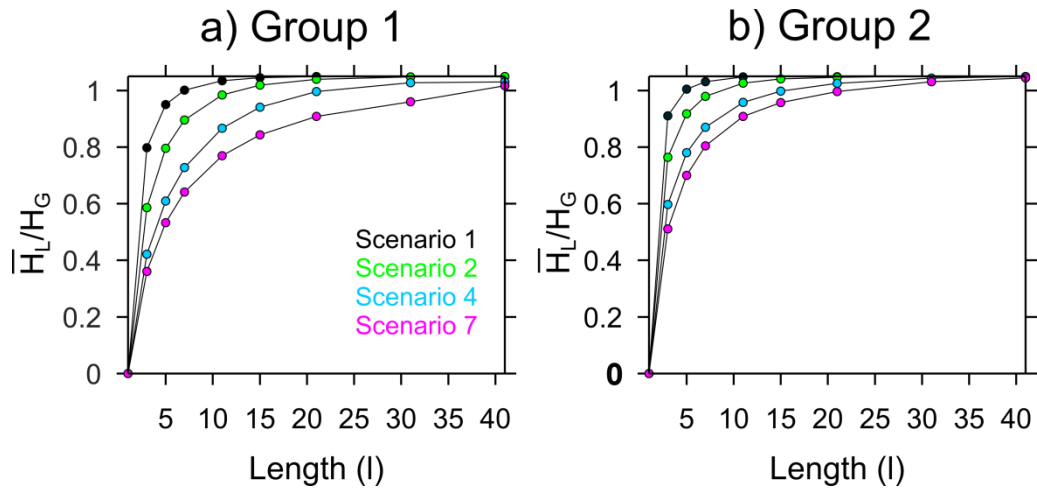


**Figure S1.** Variations of the average of the local entropy ( $H_L$ ) with respect to the length ( $l$ ) of the subdomain considered for the calculation

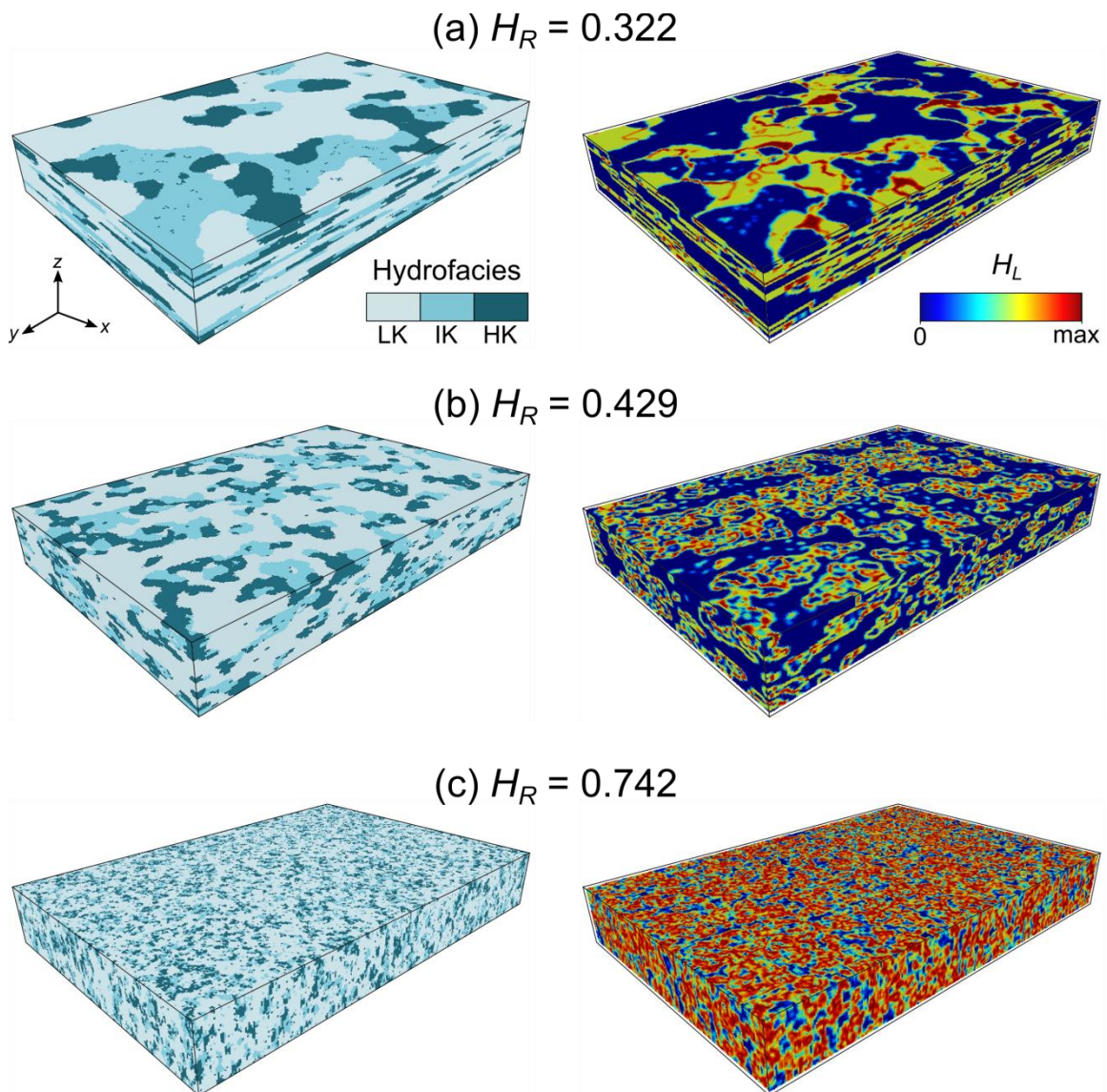


**Figure S2.** Selected scenarios of aquifer heterogeneity considered in Group 1. One realization of hydrofacies distribution for each scenario is shown to the left. Corresponding maps of local entropy ( $H_L$ ) are plotted to the right. The relative entropy index  $H_R$  provides a quantification of geological entropy for each field. Domain dimensions are specified in Figure 4 of the paper.

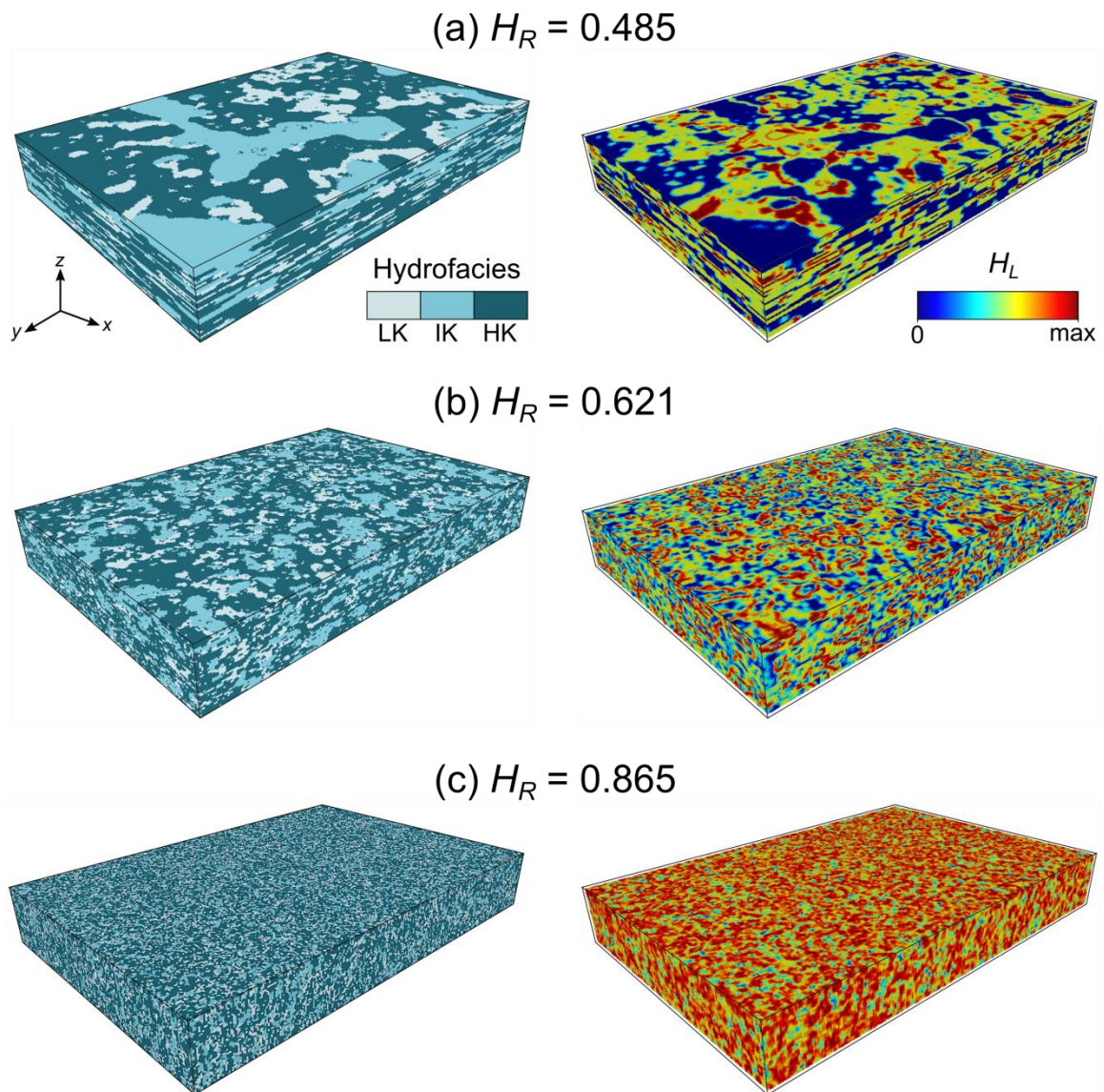


**Figure S3.** Selected scenarios of aquifer heterogeneity considered in Group 2. One realization of hydrofacies distribution for each scenario is shown to the left. Corresponding maps of local entropy ( $H_L$ ) are plotted to the right. The relative entropy index  $H_R$  provides a quantification of geological entropy for each field. Domain dimensions are specified in Figure 4 of the paper.

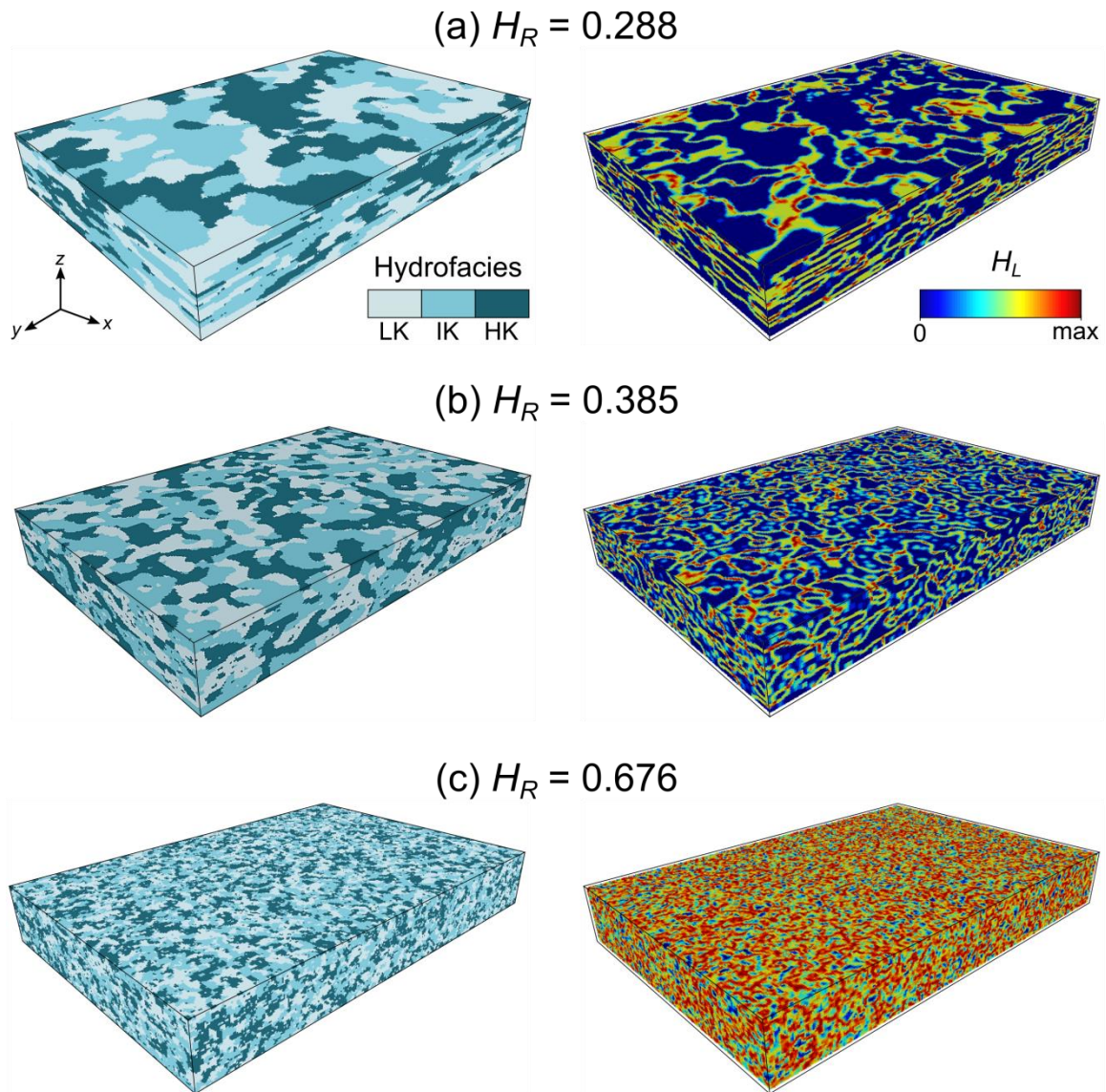


**Figure S4.** Selected scenarios of aquifer heterogeneity considered in Groups 3-5. One realization of hydrofacies distribution for each scenario is shown to the left. Corresponding maps of local entropy ( $H_L$ ) are plotted to the right. The relative entropy index  $H_R$  provides a quantification of geological entropy for each field. Domain dimensions are specified in Figure 4 of the paper.

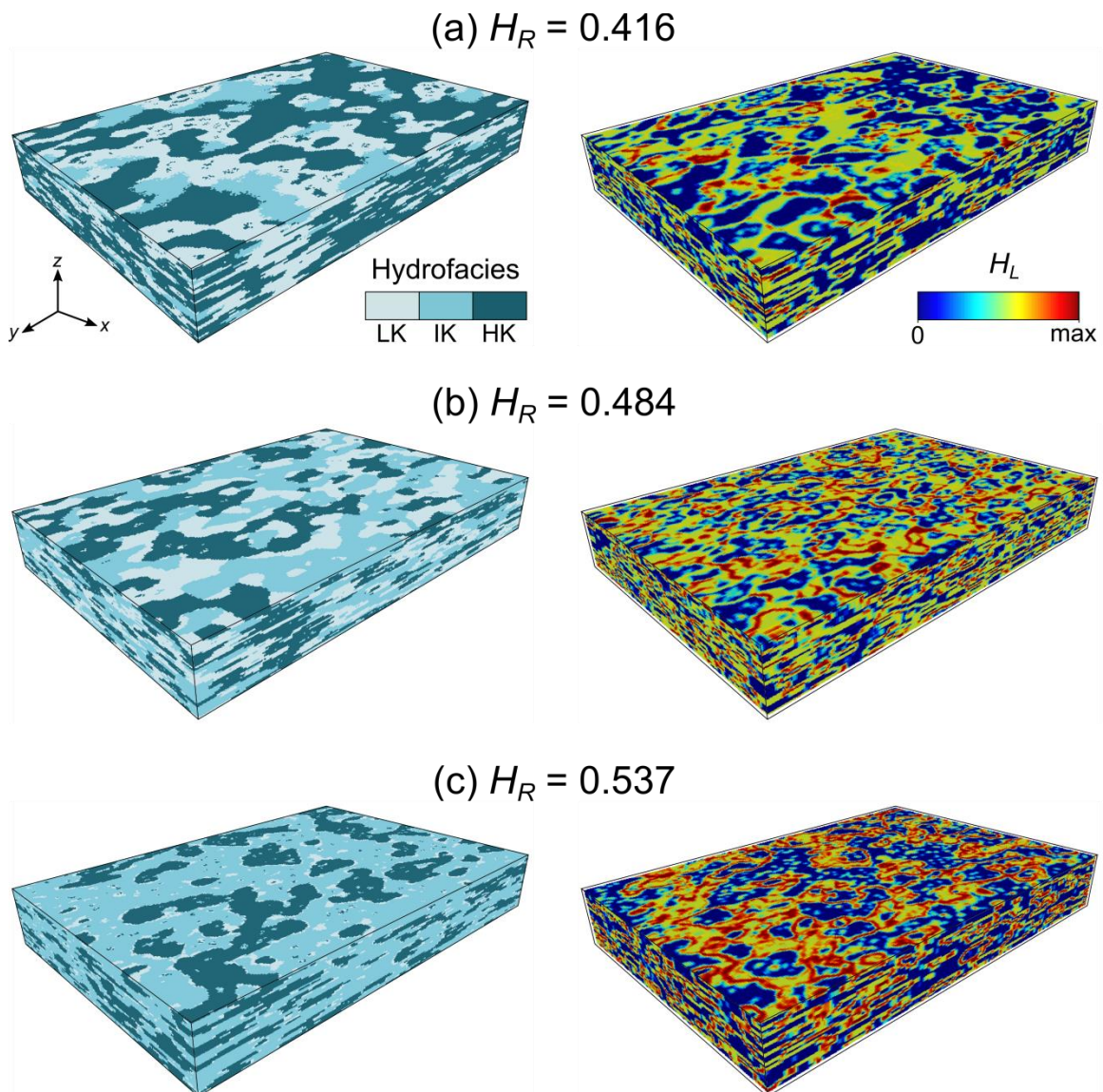


**Figure S5.** Selected scenarios of aquifer heterogeneity considered in Group 6. One realization of hydrofacies distribution for each scenario is shown to the left. Corresponding maps of local entropy ( $H_L$ ) are plotted to the right. The relative entropy index  $H_R$  provides a quantification of geological entropy for each field. Domain dimensions are specified in Figure 4 of the paper.

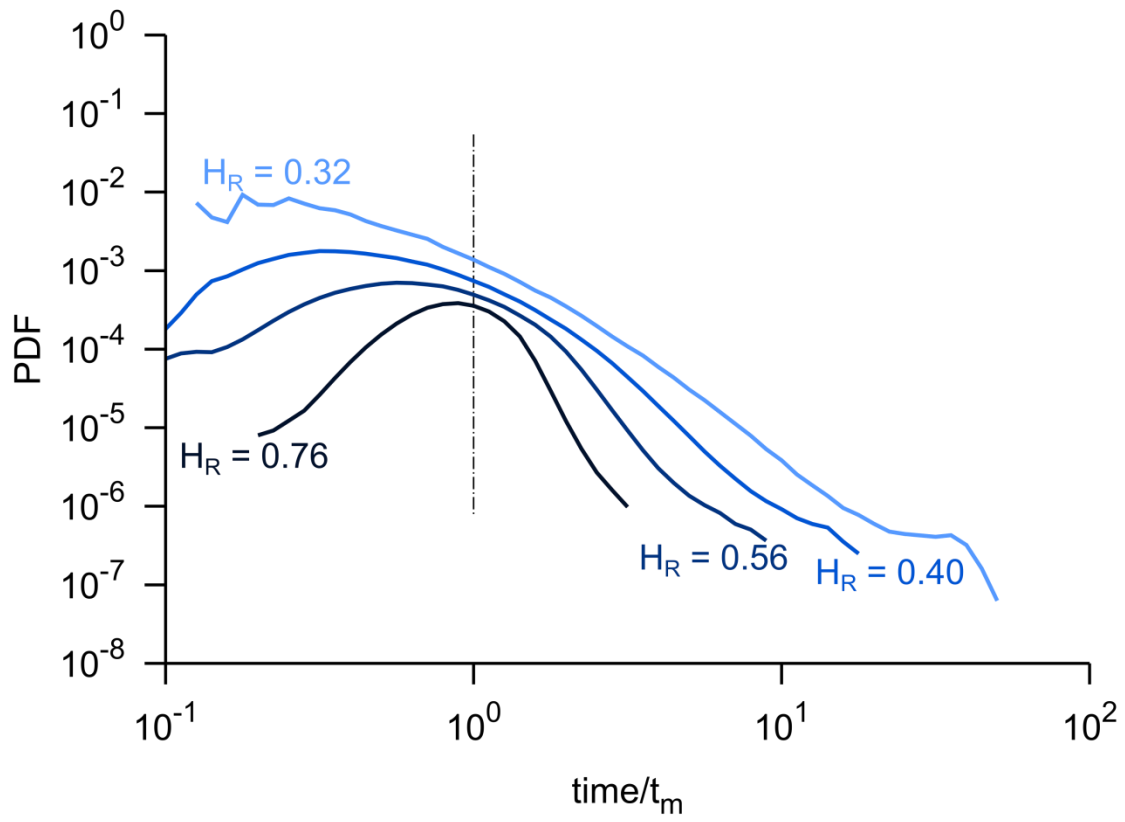


**Figure S6.** Ensemble mean breakthrough curves for selected scenarios in Group 1. Arrival times are normalized by the mean value  $t_m$ .

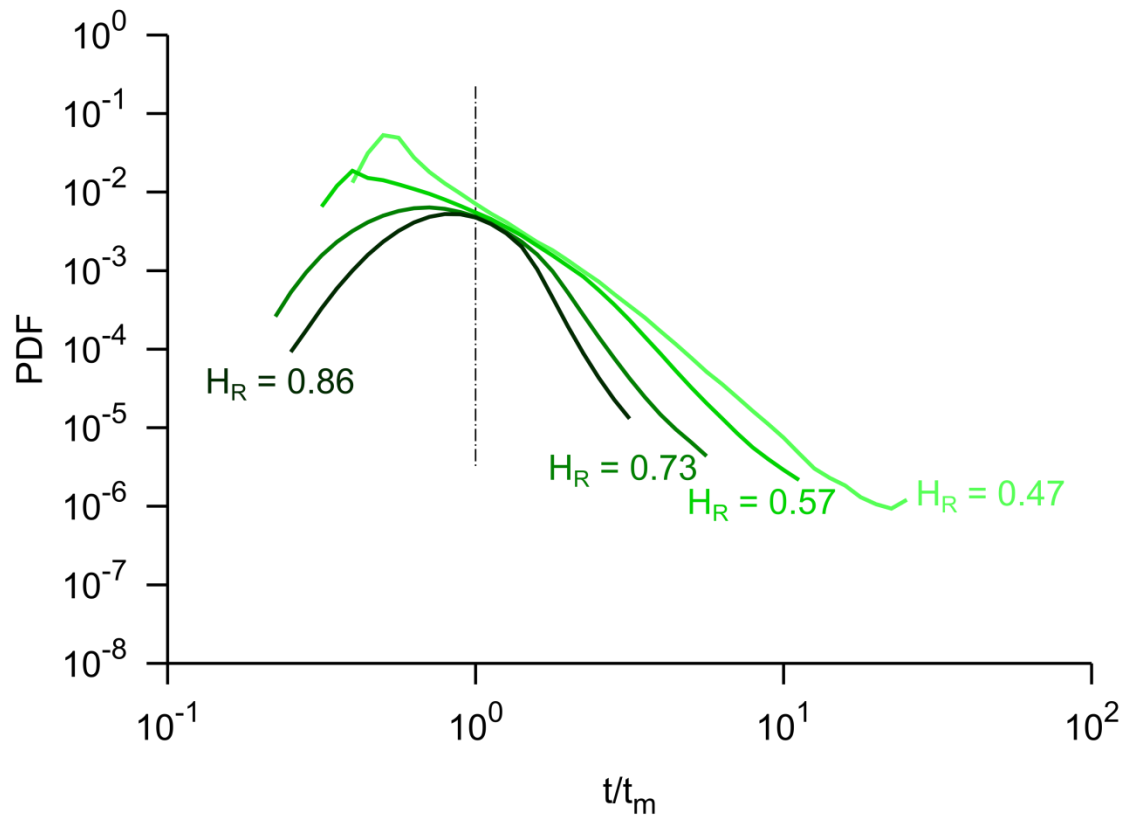


**Figure S7.** Ensemble mean breakthrough curves for selected scenarios in Group 2.

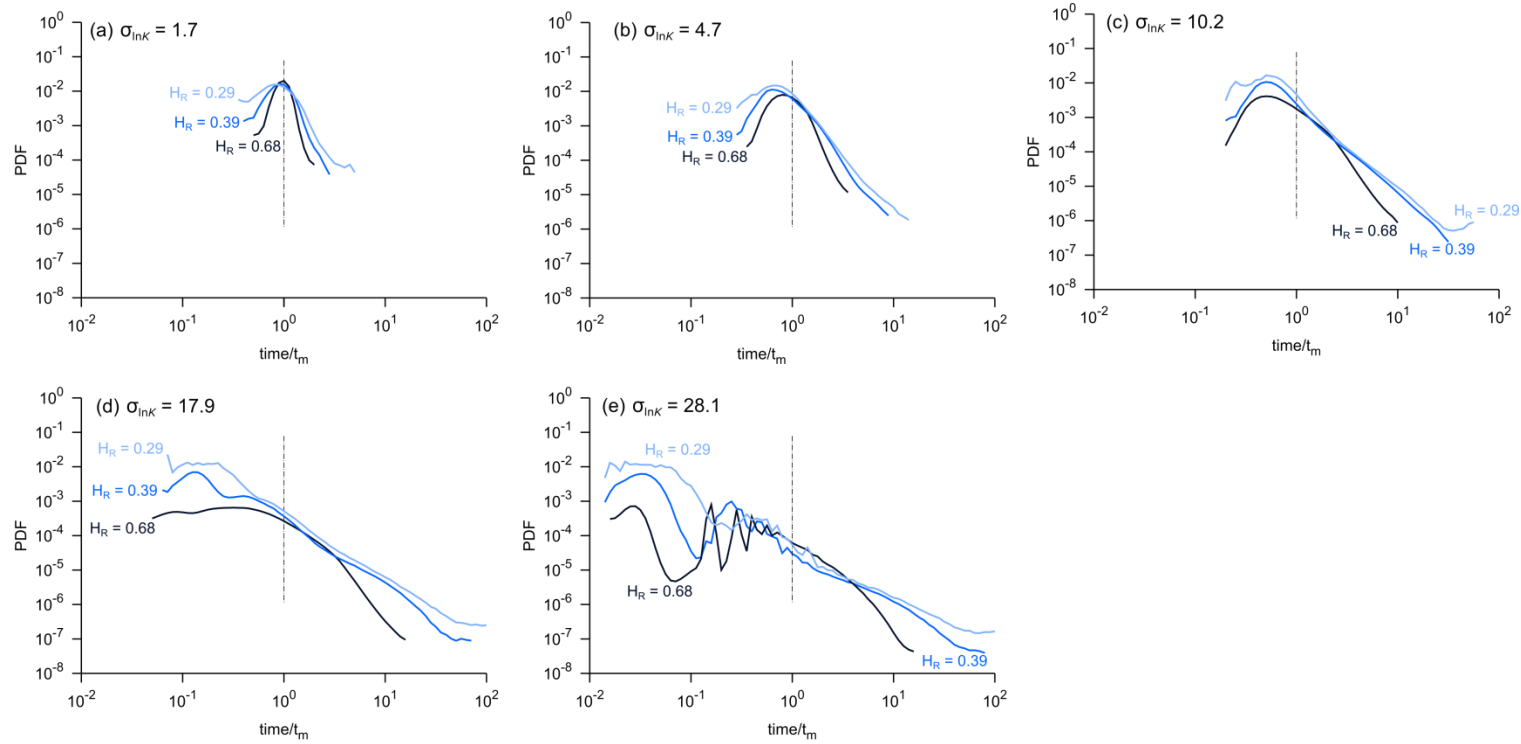


**Figure S8.** Ensemble mean breakthrough curves for selected scenarios in Groups 3, 4, and 5.

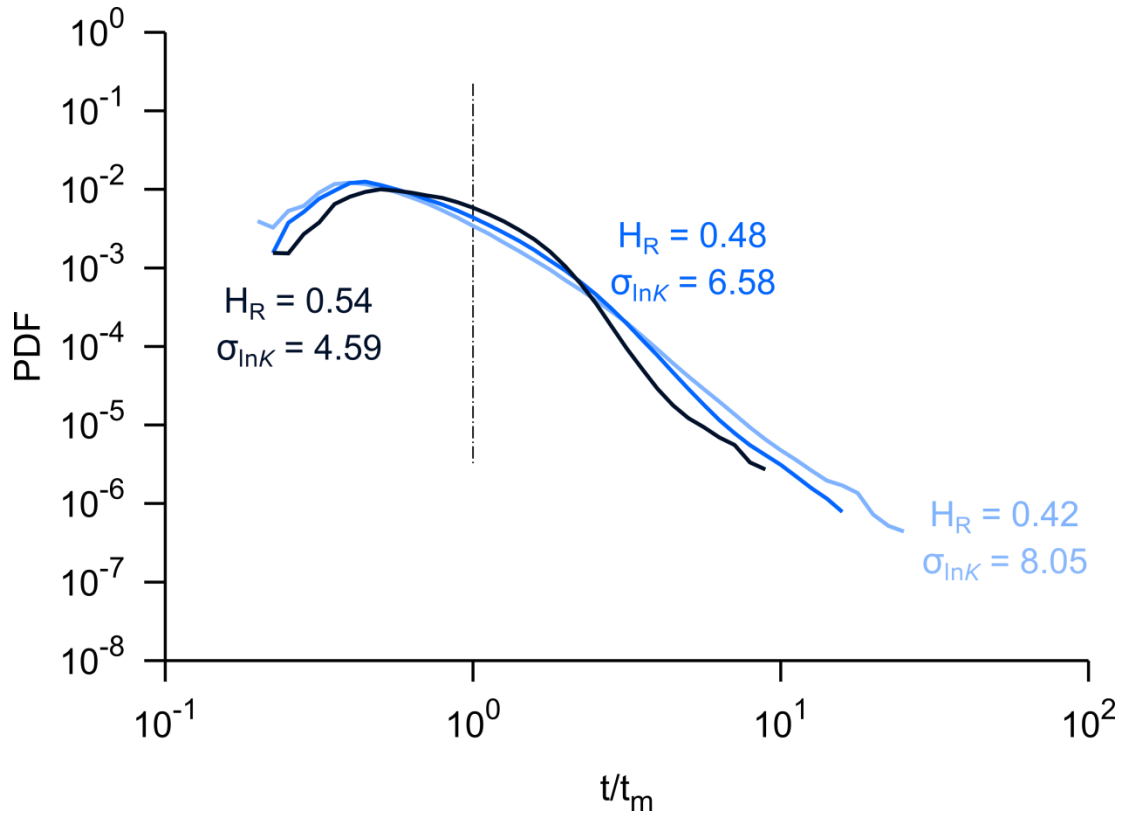


**Figure S9.** Ensemble mean breakthrough curves for selected scenarios in Group 6. Arrival times are normalized by the mean value  $t_m$ .

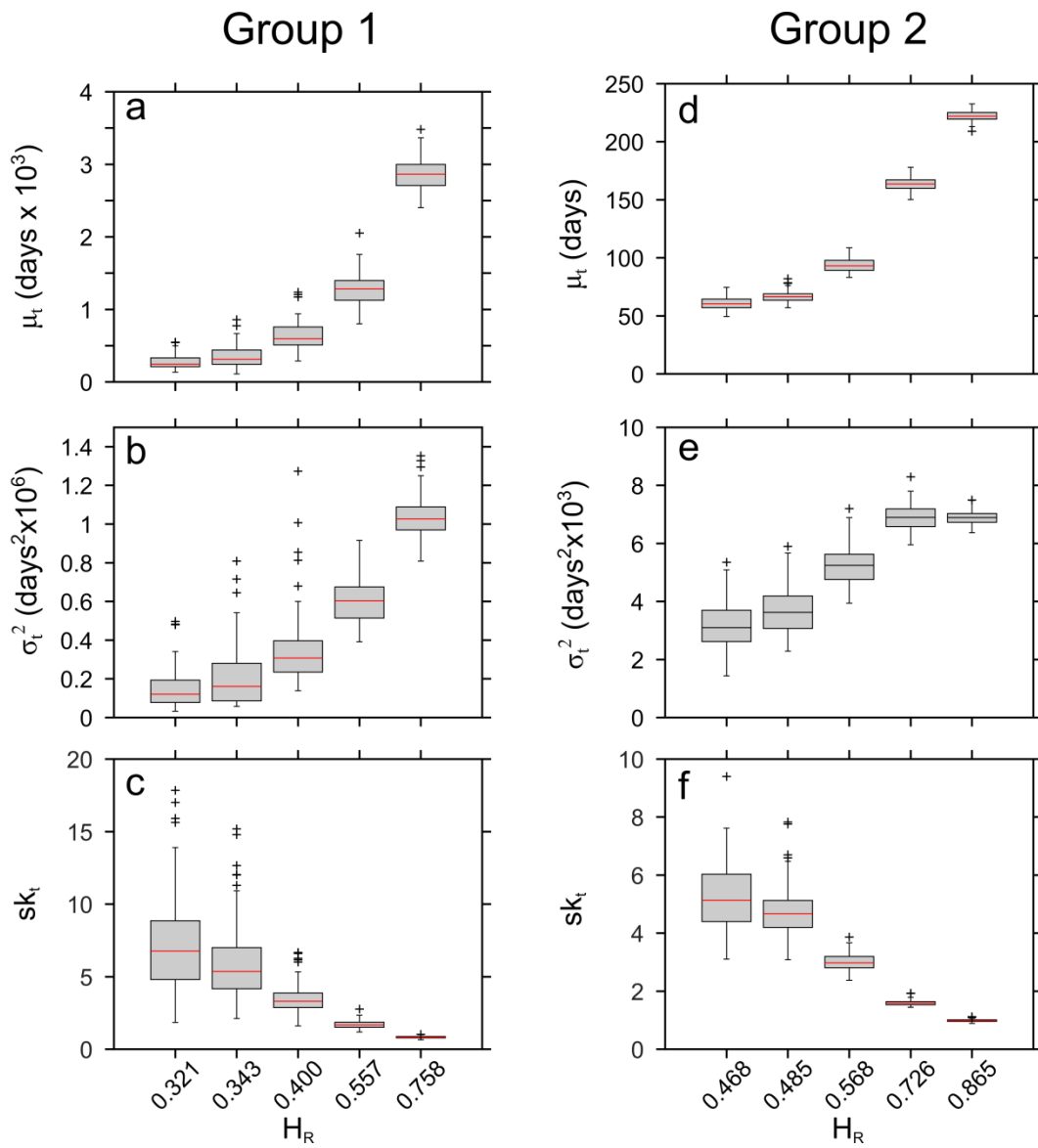


**Figure S10.** Boxplot of the distributions of the temporal moments for selected scenarios in Groups 1 and 2.

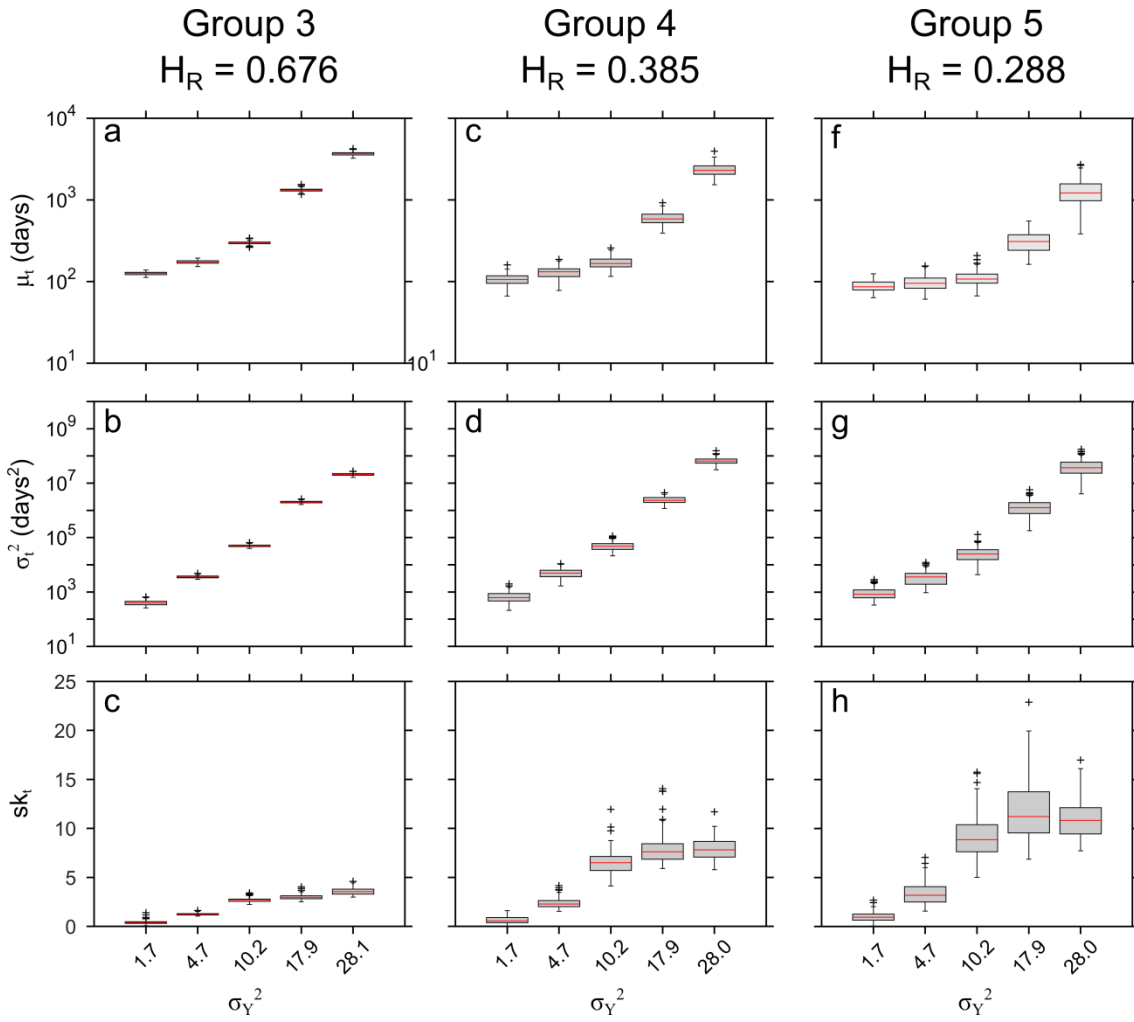


**Figure S11.** Boxplot of the distributions of the temporal moments for selected scenarios in Groups 3, 4 and 5.

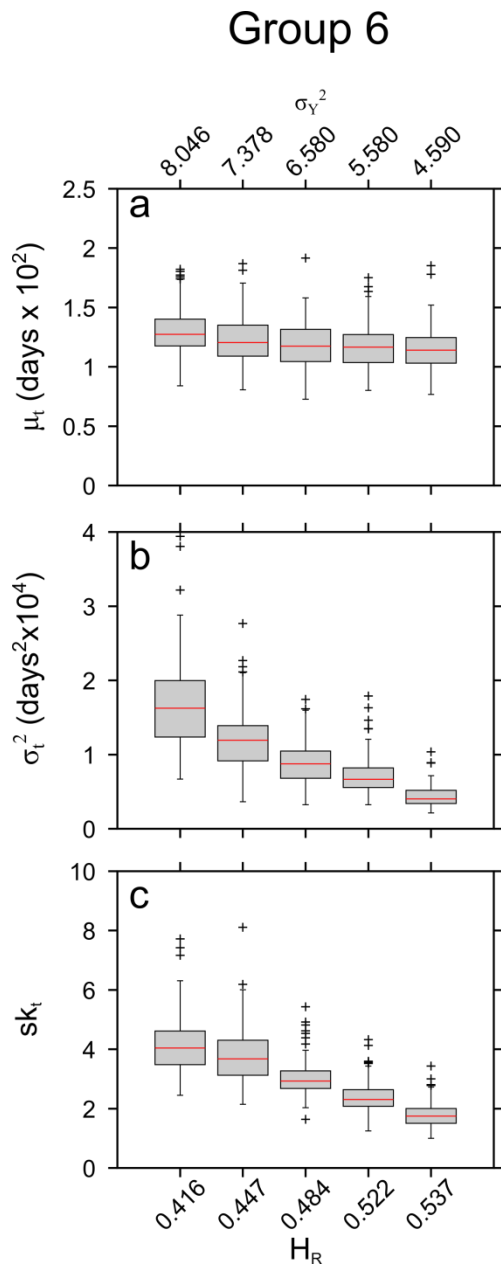


**Figure S12.** Boxplot of the distributions of the temporal moments for selected scenarios in Group 6.

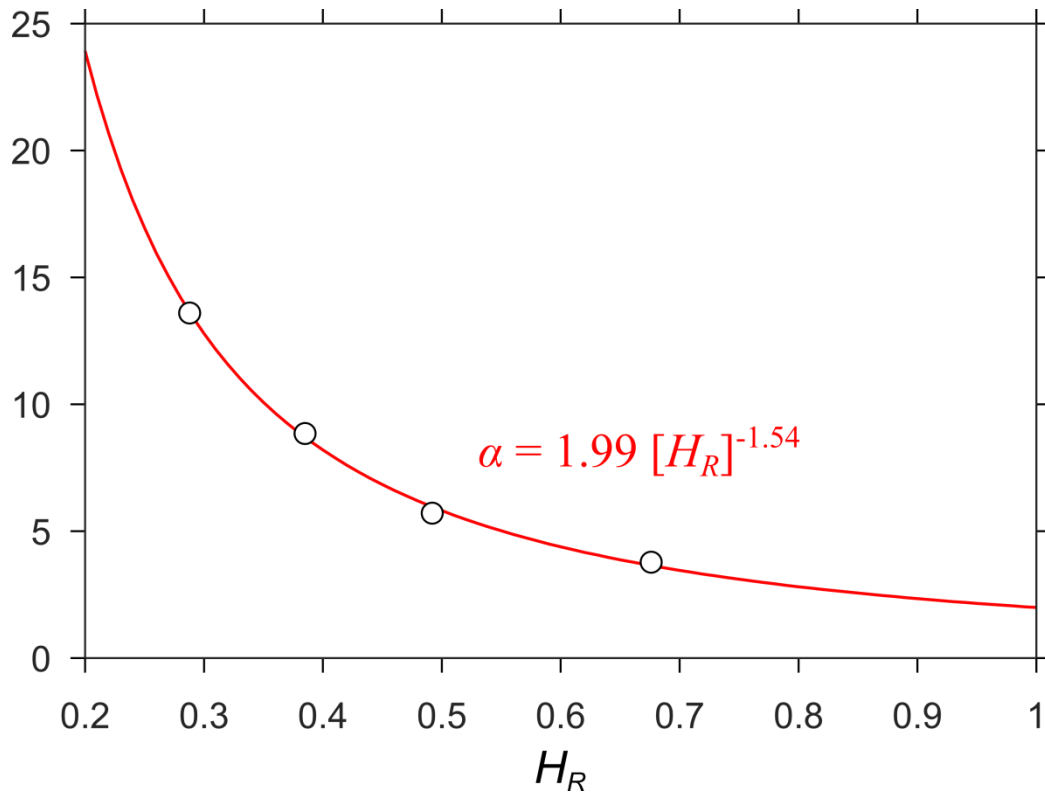


**Figure S13.** Behavior of the parameter  $\alpha$  (see Equation 13 in the paper) with  $H_R$ . Experimental data from results of transport simulations in Groups 3, 4, 5 and in another group with  $H_R = 0.5$  (not discussed in the paper) are plotted as circles. Regression line (equation provided) is plotted in red. The  $R^2$  of the regression line is 0.998.

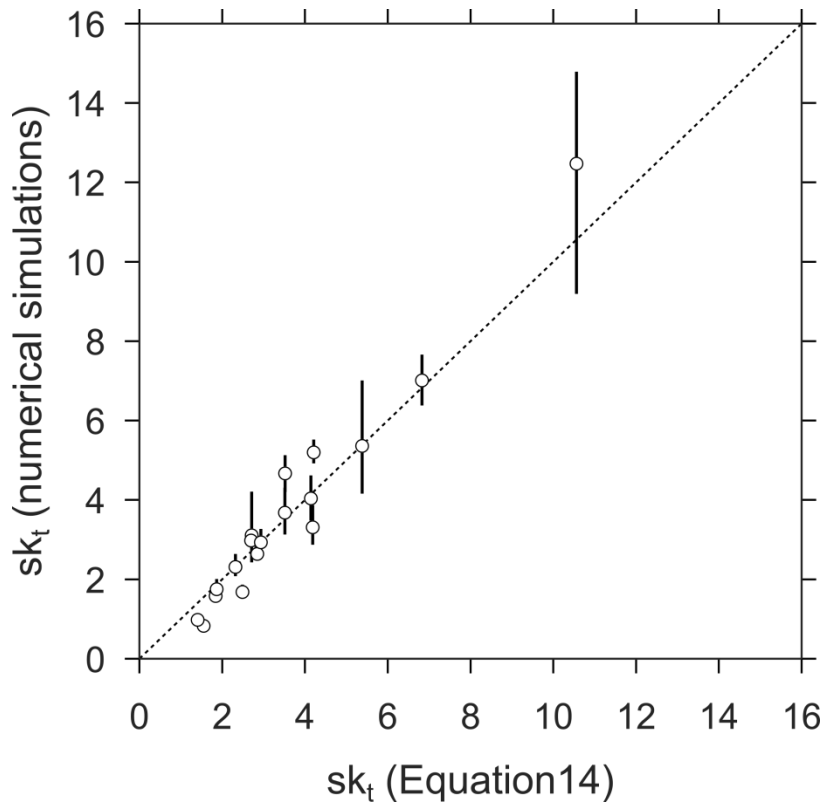


**Figure S14.** Comparison between median skewness values from numerical simulations and corresponding predicted values from the empirical expression in Equation 14 of the paper. Vertical lines indicate the interquartile range of the distributions of simulated skewness values.

## 6 Text S1: Analysis of the scenarios with variable $H_R$ and $\sigma_Y^2$ (Group 6)

In the paper, we illustrate the dependency between transport behavior and geological entropy in scenarios of aquifer heterogeneity considering variations of either  $H_R$  (Groups 1 and 2) or  $\sigma_Y^2$ . In the following, we present the results from the five scenarios of Group 6 in which we vary both heterogeneity parameters.

In this group, we assume that the volumetric proportion of hydrofacies IK varies from 1/9 (Scenario 1) to 5/9 (Scenario 5), while the volumetric proportion of hydrofacies HK is assumed equal to 1/3 in all the scenarios. For each scenario, hydrofacies LK fills the remaining volume in the 3-D domain. Accordingly, its volumetric fraction varies in the group from 5/9 (Scenario 5) to 1/9 (Scenario 1). This group is designed to investigate variations in both the structure and the bulk conductivity of the lower  $K$  matrix of the aquifer, while the spatial continuity of the highly conductive hydrofacies HK is left unchanged.

Although  $K$  contrasts between hydrofacies are assumed constant for the different scenarios, changes in the volumetric proportions of hydrofacies LK and IK result in variations of  $\sigma_Y^2$  and  $H_R$ . As shown in Figure 3c of the paper,  $H_R$  increases with the volumetric proportion of hydrofacies IK, while the variance  $\sigma_Y^2$  shows a monotonically decreasing trend. However, the overall variation of  $H_R$  is relatively moderate (29%) in comparison with the corresponding variation of  $\sigma_Y^2$  (43%).

Ensemble of solute BTCs for selected scenarios of Group 6 are plotted in Figure S9, while the boxplots of the distributions of the temporal moments of the BTCs are presented in Figure S12. Consistent with the results from the other groups, the BTCs become more asymmetric with increasing values of  $\sigma_Y^2$  and  $H_R$ . It is reasonable to ask at this point which of the two heterogeneity parameters has more impact on the transport behavior. An indication at this regard is provided by the analysis of the variations of the median values of the central temporal moments of the BTCs with respect to  $H_R$  and  $\sigma_Y^2$ . These values are plotted in Figure S15. Assuming linear correlations between the heterogeneity parameters and the median values of the moments, we can use the slopes of these linear functions as an indication of sensitivity. The higher slope values of the linear functions describing the relation between  $H_R$  and the temporal moments suggest that  $H_R$  has higher impact on transport behavior compared to  $\sigma_Y^2$ .

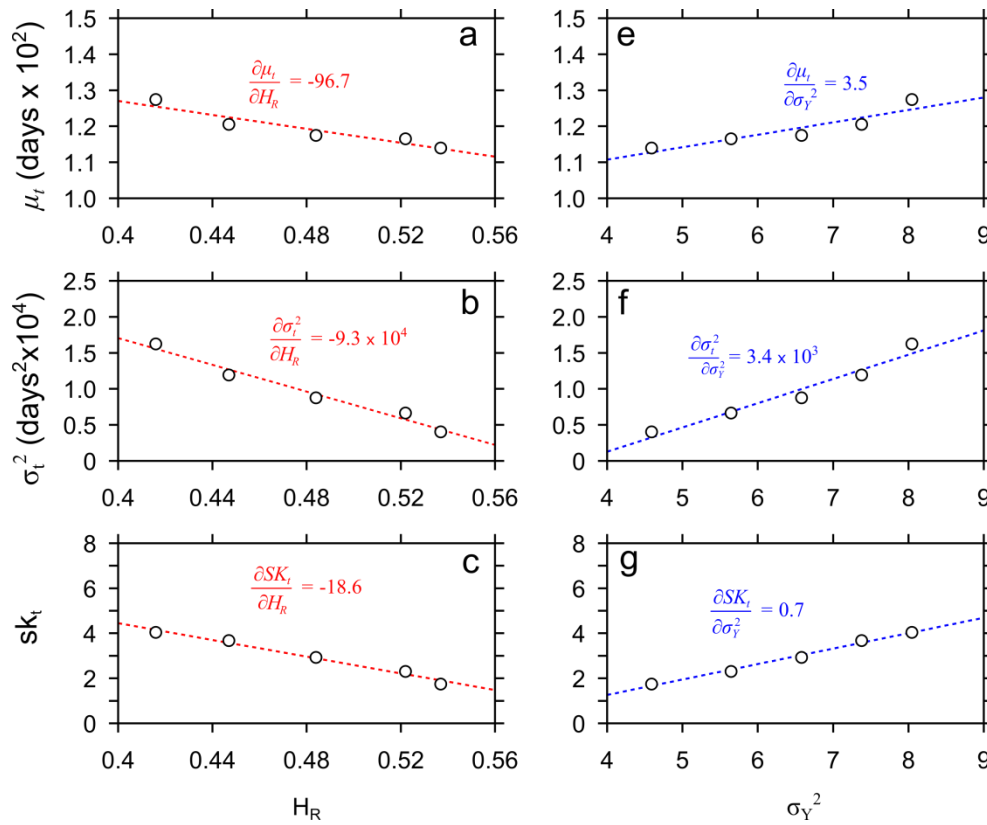


**Figure S15.** Median values of the mean ( $\mu_t$ ), the variance ( $\sigma_t^2$ ), and the skewness ( $sk_t$ ) of the BTCs for Group 6. Slopes of the linear regression lines are provided as an indication of sensitivity.